Applied Mathematical Modelling 74 (2019) 621–640

Contents lists available at ScienceDirect

Applied Mathematical Modelling

journal homepage: www.elsevier.com/locate/apm

Micro-textures inversely designed with overlayed-lithography manufacturability for wetting behavior in Cassie–Baxter status

Yongbo Deng[a,b,*], Zhenyu Liu[c], Yasi Wang[d], Huigao Duan[d], Jan G. Korvink[a,*]

[a] *Institute of Microstructure Technology (IMT), Karlsruhe Institute of Technology (KIT), Hermann-von-Helmholtzplatz 1, Eggenstein-Leopoldshafen 76344, Germany*
[b] *State Key Laboratory of Applied Optics, Changchun Institute of Optics, Fine Mechanics and Physics (CIOMP), Chinese Academy of Sciences, Changchun 130033, China*
[c] *Changchun Institute of Optics, Fine Mechanics and Physics (CIOMP), Chinese Academy of Sciences, Changchun 130033, China*
[d] *State Key Laboratory of Advanced Design and Manufacturing for Vehicle Body, College of Mechanical and Vehicle Engineering, Hunan University, Changsha 410082, China*

ARTICLE INFO

Article history:
Received 9 August 2018
Revised 13 April 2019
Accepted 30 April 2019
Available online 10 May 2019

Keywords:
Micro-texture
Inverse design
Cassie–Baxter mode
Wetting behavior
Topology optimization
Overlayed-lithography manufacturability

ABSTRACT

Robust Cassie–Baxter wettability of a rough solid surface with micro-textures is a key factor for stable hydrophobicity. Overlayed micro-textures are potentially more effective in ensuring the robustness of the surface properties, because of the layer-by-layer increase of the duty ratio and their effective approximation of the full hierarchy. However, a design methodology that includes considering manufacturability is lacking. In this article, we address this deficiency and present a monolithic inverse design approach, composed of a series of topology optimizations, to derive micro-textures with hierarchy approximated by overlayed geometries. The optimization are implemented in a dimensionless manner using a periodic regular-polygon tiling of the plane, in which the corresponding dimensionless Young-Laplace equation is used to describe the physics at the liquid/vapor interface. Two sequential and neighboring optimization tasks are linked through the design domain of the downward layer, determined by a conformal extension of the physical density representing the pattern of the upward layer. This ensures the manufacturability e.g. for an overlayed lithography process. Layer-by-layer robustness enhancement is thereby achieved, and the capability to anchor the three-phase contact line after the collapse of the liquid/vapor interface supported by the upward layer. In generating the overlayed micro-textures, a rigorous scaling factor for the patterns was determined, leading to a recursion inequality based on the depth of the liquid/vapor interfaces at the critical static pressures that determines the extrusion distance of the patterns. The trace height and minimal aspect ratio of the micro-textures are specified by the scaling factor and extrusion distance for a layer. This allows a compromise between performance and manufacturability, and thereby avoid instabilities caused by elasto-capillary collapse of the micro-/nano-structures. We computationally confirm the optimality by comparing the derived micro-textures with previously reported designs.

---

* Corresponding author.
E-mail addresses: yongbo.deng@kit.edu, dengyb@ciomp.ac.cn (Y. Deng), liuzy@ciomp.ac.cn (Z. Liu), jan.korvink@kit.edu (J.G. Korvink).

https://doi.org/10.1016/j.apm.2019.04.059
0307-904X/© 2019 Elsevier Inc. All rights reserved.

1. Introduction

Wettability of a solid surface is determined by its geometrical morphology and surface free energy [1]. For a given substrate, the wetting behavior is dominated by micro-textures, because micro-textures on a solid surface can effectively change the surface free energy. On a solid surface with micro-textures, two different solid/liquid contact modes can exist, i.e., the Wenzel and Cassie–Baxter modes [2,3]. In the Wenzel mode, the liquid completely fills the micro-textures; in the Cassie–Baxter mode, vapor pockets are trapped by the liquid/vapor interface supported by the micro-textures, so that the solid surface presents to the liquid a composite of solid and vapor patches. The solid/liquid contact mode can transfer from a Cassie–Baxter case to the Wenzel case, when the liquid is physically pressed into the cavities [4,5]. In this mode transition process, the surface free energy decreases along with the liquid filling the micro-textures. The access to controlled wettability profiles via the Cassie–Baxter mode has numerous applications in the areas of micromechanics [6], super-hydrophobicity [7], anti-drag [8], lubrication [8,9], microelectromechanical systems [10], microfluidics [11], electrohydrodynamics [12], separation of oil and water [13,14], self-cleaning coatings [15], etc. Therefore, it would be advantageous to bring rational design to wettability texturing.

The use of artificial micro-textures for Cassie–Baxter modes on a solid surface has been previously reported. To create micro-textures, circular posts, square posts, and tapered-cone structures are widely used periodic units [16–21]. Inspired by nature, e.g., lotus leaves and water-strider legs, bio-inspired hierarchical micro-textures have been variously discussed in [22–29], and have been extended for use in liquid-solid adhesion [30]. The theory, design, and applications for micro-textures have been summarized in [31]; especially, the inverse design method has been developed for micro-textures with a single-layer instead of an overlayed geometry [32,33]. Compared to micro-textures formed from posts with regular cross-sections, hierarchical micro-textures are potentially more robust and effective, because of their hierarchy with the affordability for multiple critical static pressure. The periodic units of hierarchical micro-textures usually have complicated geometrical configurations, and hence bottom-up processes (e.g. self-assembly) have been developed for their fabrication [34,35]. In contrast, fully developed and overlayed photolithography-like top-down processes can ensure more accurate and consistent periodic units of the hierarchical micro-texture [36]. The overlayed geometry for the corresponding process is an effective approximation for the full hierarchy. The degree of approximation can be enhanced by increasing the number of layers. To date, a rational design procedure is lacking that specifically targets the overlayed manufacturability of hierarchical morphologies for widely available photolithography-like manufacturing processes. Therefore, this article addresses this deficiency, by focusing on achieving a novel inverse design tool, in which the geometrical configurations in the overlayed hierarchy are obtained from a monolithic inverse design approach composed of a series of sequentially implemented and coupled topology optimizations.

Topology optimization, a full-parameter method, can inversely determine the geometrical configurations of structures [37]. In contrast to designing devices by tuning a handful of structural parameters, it utilizes a continuous parameter space to design structures solely based on the users' specification of the desired structural performance. Thereby, topology optimization can inversely and simultaneously find a reasonable structural shape and topology. It is thus a more general computational design method than mere shape optimization, which usually improves the performance of a device by adjusting the structural boundaries, keeping the topology of the structure invariant. On the other hand, topology optimization can also ensure the manufacturability of the found structure through the use of additional constraints [38]. And this method has been extended to multiple physical problems, e.g. acoustics, electromagnetics, fluidic dynamics, optics, thermodynamics, and material design problems [39–51]. It will therefore be our chosen methodology for designed wetting behaviour.

The rest of this article is organized as follows. In Section 2, the inverse design method is introduced for the periodic units of the micro-textures with overlayed-lithography manufacturability. In Section 3, the micro-textures with overlayed geometries are derived and discussed. It is concluded in Section 4, acknowledged in Section 5. and appendixed in Appendix A.1.

2. Method

Because micro-textures on a solid surface usually exist with some degree of periodicity [52], this aspect is now considered for wettability in the Cassie–Baxter mode. For the regular-polygon periodicity of the pattern, either a regular triangle, a quadrangle, or a hexagon can be used to completely tile a flat solid surface without overlap, where the regular-triangle tiling involves a rotation in addition to a translation operation (Fig. 1). The three periodic units can be further reduced to three differently shaped irreducible triangles in normalized size, based on the given symmetries (Fig. 2). By considering the performance and overlayed lithography-like manufacturability of the micro-textures, the inverse design is sequentially implemented on each irreducible triangular-domain, in order to achieve patterns of layers in a ceiling-to-floor order. The geometrical configuration of the final micro-textures is then obtained by reflection, scaling, extrusion, piling and paving operations of the computed patterns, and this generation procedure is demonstrated in Appendix A.1. In this procedure, the pattern for the ceiling layer featuring the smallest duty ratio is inversely designed firstly. Subsequently, a pattern for next down remaining layer is inversely designed in a domain obtained by removing the subdomain formed by a conformal lateral extension of the pattern from the upward neighboring layer. The conformal extension is utilized to implement a sidestep between the two neighboring layers, for which extrusion and pile operations are implemented. The sidestep will anchor the three-phase contact lines at each position without having branch micro-textures connected, to ensure that a liquid/vapor interface is completely suspended by the corresponding layer. This procedure will also ensure that the ceiling layer, with

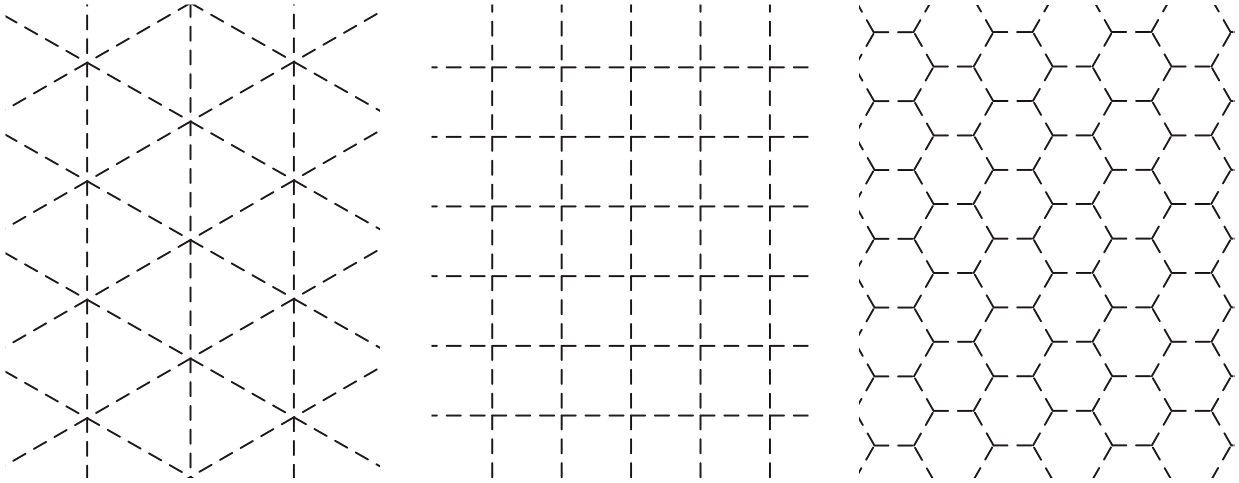
(a) (b) (c)

Fig. 1. Demonstration of the tiling of a flat solid surface, using a regular (a) triangle, (b) quadrangle, (c) and hexagon.

the smallest duty ratio, features an optimal performance and robustness of the Cassie–Baxter mode, but which increases layer-by-layer because of the additional incremental duty ratios in the ceiling-to-floor direction.

2.1. Modeling based on topology optimization method

For wetting behavior in the Cassie–Baxter mode, with a liquid/vapor interface loaded to a fixed static pressure, the reasonability of a given micro-texture can be measured by the liquid-bulge volume supported on the liquid/vapor interface. A smaller liquid-bulge volume corresponds to a more robust Cassie–Baxter mode. A larger liquid-bulge volume could threaten to overwhelm the surface tension, resulting in the wetting of the entire solid surface. Therefore, the micro-textures on a solid surface should be inversely designed by finding the surface topology that minimizes the liquid-bulge volume suspended on the liquid/vapor interface.

Under equilibrium conditions, the liquid/vapor interface suspended on the periodic micro-texture is a two-dimensional (2D) manifold with constant Riemann curvature, and can be described by the dimensionless Young-Laplace equation defined on one of the irreducible triangles in Fig. 2 [53,54]:

$$\begin{aligned}
&\nabla\cdot\left(\bar{\sigma}\frac{\nabla\bar{z}^{(i)}}{\sqrt{(L/z_0)^2+\left|\nabla\bar{z}^{(i)}\right|^2}}\right)=1,\ \text{in }\Omega\\
&\bar{\sigma}\frac{\nabla\bar{z}^{(i)}}{\sqrt{(L/z_0)^2+\left|\nabla\bar{z}^{(i)}\right|^2}}\cdot\mathbf{n}=0,\ \text{on }\partial\Omega\\
&\bar{z}^{(i)}=0,\ \text{at }O
\end{aligned}\tag{1}$$

where $\bar{z}^{(i)}=z^{(i)}/z_0,\ i\in\{1,2,\ldots,N\}$ is the normalized vertical coordinate of the interface supported by the ith layer of the overlayed micro-texture, with $z^{(i)}$ representing the magnitude of the original vertical coordinate and N representing the number of layers; L is the lattice constant of the periodic unit, and is defined to be the center-to-center distance between two neighboring periodic units; $\bar{\sigma}=\sigma/(LP)$ is the dimensionless surface tension, with σ the surface tension and P the static pressure at the liquid/vapor interface; ∇ is the gradient operation defined on the xOy plane, with O the coordinate origin; Ω is an irreducible triangular-domain; $\mathbf{n}$ is the outward unit normal on the boundary. To ensure uniqueness of the solution, the liquid/vapor interface is constrained at the coordinate origin, which simultaneously is the minimal constraint introduced for Eq. (1). The liquid/vapor interfaces described by Eq. (1) are constant-curvature 2D manifolds defined on the three irreducible triangles, as sketched in Fig. 3.

Based on the above mathematical description, the boundaries of the liquid/vapor interface are completely localized in the xOy plane. This interface is a 2D manifold with uniform convexity, which can be measured by the volume enclosed by the interface and the xOy plane, i.e., the liquid-bulge volume supported by the micro-texture over an irreducible triangle. This volume is calculated to be $z_0L^2\left|\int_\Omega\bar{z}^{(i)}\,\mathrm{d}\Omega\right|$. $\left|\int_\Omega\bar{z}^{(i)}\,\mathrm{d}\Omega\right|$ and $\left(\int_\Omega\bar{z}^{(i)^2}\,\mathrm{d}\Omega\right)^{\frac{1}{2}}$ are two different norms of $\bar{z}^{(i)}\in\mathcal{H}(\Omega)$, where $\mathcal{H}(\Omega)$ is the first order Hilbert functional space defined on Ω. According to the equivalence of norms [55], $\left|\int_\Omega\bar{z}^{(i)}\,\mathrm{d}\Omega\right|^2$ is equivalent to $\int_\Omega\bar{z}^{(i)^2}\,\mathrm{d}\Omega$; hence, minimizing $\int_\Omega\bar{z}^{(i)^2}\,\mathrm{d}\Omega$ is equivalent to enhancing the robustness of the Cassie–Baxter mode.

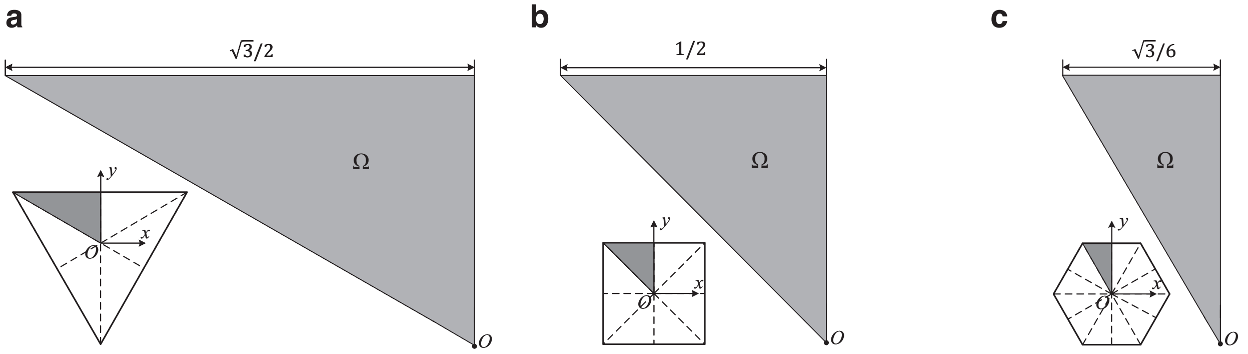

Fig. 2. Irreducible triangular-domains (represented by Ω) of dimensionless counterparts corresponding to tiles in the shape of a regular (a) triangle, (b) quadrangle, and (c) hexagon.

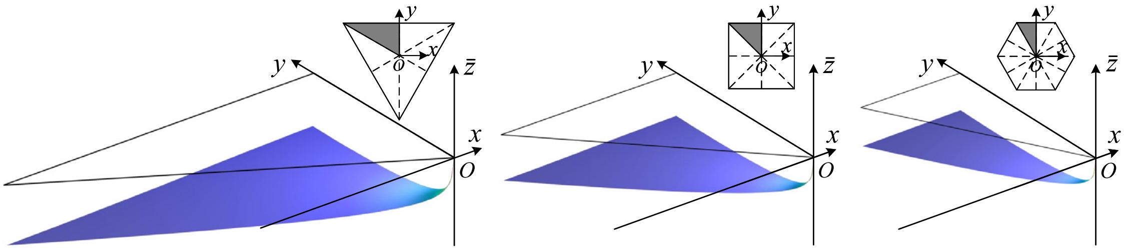

(a) (b) (c)

Fig. 3. Sketch of the liquid/vapor interfaces described by Eq. (1) defined on the three irreducible triangles in Fig. 2.

Therefore, the well-posed expression $\int_{\Omega} \bar{z}^{(i)^2} \, d\Omega / |\Omega|$, defined as liquid-bulge measurement, is preferred for the minimization, where $|\Omega|$ represents the area of Ω.

A series of variational problems can be constructed based on the topology optimization method, to determine the pattern for individual layers of the micro-textures. In the variational problem, design variables are defined on the irreducible triangles to represent the layered patterns of the micro-textures, by interpolating the dimensionless surface tension; they are valued continuously in [0, 1], with 0 and 1 respectively representing micro-texture and blankness. The number of design variables is the same as that of the number of layers in the micro-texture. Each variational problem can be iteratively solved using a numerical optimization procedure. The design variables are penalized and converged to binary distributions, corresponding to the seeked patterns. To ensure the numerical stability, we smooth the design variables using a Helmholtz filter [56]

$$\begin{cases} -\nabla \cdot \left(r_f^2 \nabla \gamma_f^{(i)} \right) + \gamma_f^{(i)} = \gamma^{(i)}, \text{ in } \Omega \\ -r_f^2 \nabla \gamma_f^{(i)} \cdot \mathbf{n} = 0, \text{ on } \partial\Omega \\ \gamma_f^{(i)} = 0, \text{ at } O. \end{cases} \tag{2}$$

Furthermore, the smoothed design variables are projected by the threshold method [57,58]

$$\gamma_p^{(i)} = \frac{\tanh(\beta\xi) + \tanh\left(\beta\left(\gamma_f^{(i)} - \xi\right)\right)}{\tanh(\beta\xi) + \tanh(\beta(1-\xi))}, \tag{3}$$

where $\gamma^{(i)}$ is the design variable for the i-th layer of the micro-texture; $\gamma_f^{(i)}$ and $\gamma_p^{(i)}$ are the filtered and projected counterparts of $\gamma^{(i)}$; r_f is the radius of the Helmholtz filter, and it is used to control the feature size of the micro-textures; β and ξ are the projection parameters with values chosen based on numerical experiments [58]. The projected design variables replace the design variables to implement the interpolation of the surface tension:

$$\bar{\sigma} = \bar{\sigma}_l + (\bar{\sigma}_s - \bar{\sigma}_l) \frac{q\left(1 - S^{(i)}\gamma_p^{(i)}\right)}{q + S^{(i)}\gamma_p^{(i)}}, \tag{4}$$

where $1 - S^{(i)}\gamma_p^{(i)}$ is the physical density for the ith layer of the micro-texture; $S^{(i)}$ is a binary distribution used to indicate the design domain of the ith layer; it is 0 on the non-designable domain of the ith layer, and 1 on the complementary

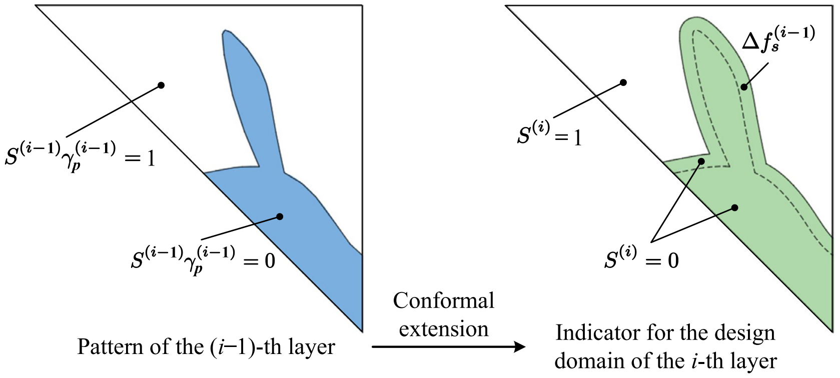

Fig. 4. Sketch of the indicator for the design domain of the *i*th layer of a micro-texture, where the indicator is determined by a conformal extension of the pattern corresponding to the physical density for the $(i-1)$th layer.

domain; $\bar{\sigma}_l$ is the dimensionless surface tension at the liquid-vapor interface; $\bar{\sigma}_s$ is the dimensionless surface tension at the top of the micro-texture; q is the parameter used to tune the convexity of this interpolation, and it is valued to be 10^{-4} based on numerical tests. Theoretically, $\bar{\sigma}_s$ should be infinite to approximate a flat liquid-solid interface; numerically, it is chosen to have a finite value of $10^5\bar{\sigma}_l$, satisfying $\bar{\sigma}_s \gg \bar{\sigma}_l$, to ensure the stability of the numerical implementation. The indicator $S^{(i)}$ is determined by a conformal extension of the pattern corresponding to $S^{(i-1)}\gamma_p^{(i-1)}$ for the $(i-1)$-th layer of the micro-texture, where the duty ratio of the extended part is $\Delta f_s^{(i-1)}$ (Fig 4). For the ceiling layer with $i = 1$, the indicator is set to $S^{(i)}|_{\forall \mathbf{x} \in \Omega} = 1$ with $\Delta f_s^{(0)} = 0$. For the other layers, it is determined by a heuristic bisection-procedure described in Appendix A.2.

Based on the presented method, the variational problem used to inversely design the patterns for the overlayed micro-textures is constructed to be a topology optimization sequence:

$$\begin{aligned}
&\text{For } i = 1, 2 \cdots N,\\
&\text{find } \gamma^{(i)}(\mathbf{x}) \in [0,1] \text{ with } \forall \mathbf{x} \in \Omega,\\
&\text{to minimize } \frac{J^{(i)}}{J_0} \text{ with } J^{(i)} = \frac{1}{|\Omega|}\int_\Omega \bar{z}^{(i)^2}\,\mathrm{d}\Omega, \text{ constrained by}\\
&\begin{cases}
\begin{cases}
\nabla \cdot \left(\bar{\sigma}\dfrac{\nabla \bar{z}^{(i)}}{\sqrt{(L/z_0)^2 + \left|\nabla \bar{z}^{(i)}\right|^2}}\right) = 1, \text{ in } \Omega\\
\bar{\sigma}\dfrac{\nabla \bar{z}^{(i)}}{\sqrt{(L/z_0)^2 + \left|\nabla \bar{z}^{(i)}\right|^2}} \cdot \mathbf{n} = 0, \text{ on } \partial\Omega \quad \text{(Young – Laplace equation)}\\
\bar{z}^{(i)} = 0, \text{ at } O
\end{cases}\\
\begin{cases}
-\nabla \cdot \left(r_f^2 \nabla \gamma_f^{(i)}\right) + \gamma_f^{(i)} = \gamma^{(i)}, \text{ in } \Omega\\
-r_f^2 \nabla \gamma_f^{(i)} \cdot \mathbf{n} = 0, \text{ on } \partial\Omega \qquad \text{(Helmholtz filter)}\\
\gamma_f^{(i)} = 0, \text{ at } O
\end{cases}\\
\gamma_p^{(i)} = \dfrac{\tanh(\beta\xi) + \tanh\left(\beta\left(\gamma_f^{(i)} - \xi\right)\right)}{\tanh(\beta\xi) + \tanh(\beta(1-\xi))} \quad \text{(Threshold projection)}\\
\left|f_d^{(i)} - f_0^{(i)}\right| \le 10^{-3}, \text{ with } f_d^{(i)} = \frac{1}{|\Omega|}\int_\Omega 1 - S^{(i)}\gamma_p^{(i)}\,\mathrm{d}\Omega \quad \text{(Duty ratio)}
\end{cases}
\end{aligned} \tag{5}$$

where a duty-ratio constraint is imposed on the *i*th layer of the micro-texture, with $f_d^{(i)}$ representing the duty ratio and $f_0^{(i)} \in (0,1)$ representing the specified duty ratio with a permitted tolerance of 10^{-3}; J_0 is the liquid-bulge measurement value corresponding to the periodic regular triangle, quadrangle or hexagon posts with specified duty ratio $f_0^{(1)}$. The patterns in the reduced triangular-domains can be inversely designed sequentially for the micro-textures from its ceiling to floor layer, by solving the variational problem in Eq. (5) with a specified duty-ratio $f_0^{(i)}$ on a corresponding design domain indicated by $S^{(i)}$ as obtained from the extension of the pattern corresponding to $S^{(i-1)}\gamma_p^{(i-1)}$.

2.2. Analyzing the variational problem

To solve the variational problem in Eq. (5), a gradient-based iterative procedure can be used, where the gradient of the liquid-bulge measurement and duty ratio can be found by a Lagrangian multiplier-based adjoint method [59]. The gradient of the liquid-bulge measurement is

$$\frac{\delta J^{(i)}}{J_0} = \frac{1}{J_0}\int_\Omega -\gamma_{fa}^{(i)}\delta\gamma^{(i)}\,\mathrm{d}\Omega \tag{6}$$

where $\delta J^{(i)}$ and $\delta\gamma^{(i)}$ are the first-order variations of $J^{(i)}$ and $\gamma^{(i)}$, respectively; $\gamma_{fa}^{(i)}$ is the adjoint variable of the filtered design variable $\gamma_f^{(i)}$. $\gamma_{fa}^{(i)}$ in Eq. (6) is found by sequentially solving the weak adjoint equations of the Young–Laplace equation and Helmholtz filter:

$$\text{Find } \bar{z}_a^{(i)} \in \mathcal{H}(\Omega) \text{ with } \bar{z}_a^{(i)} = 0 \text{ at } O, \text{ satisfying}$$

$$\int_\Omega \frac{2}{|\Omega|}\bar{z}^{(i)}\tilde{\bar{z}}_a^{(i)} - \bar{\sigma}\frac{\nabla\bar{z}_a^{(i)}\cdot\nabla\tilde{\bar{z}}_a^{(i)}}{\sqrt{(L/z_0)^2+\left|\nabla\bar{z}^{(i)}\right|^2}} + \bar{\sigma}\frac{\left(\nabla\bar{z}^{(i)}\cdot\nabla\bar{z}_a^{(i)}\right)\left(\nabla\bar{z}^{(i)}\cdot\nabla\tilde{\bar{z}}_a^{(i)}\right)}{\left(\sqrt{(L/z_0)^2+\left|\nabla\bar{z}^{(i)}\right|^2}\right)^3}\,\mathrm{d}\Omega = 0,\ \tilde{\bar{z}}_a^{(i)} \in \mathcal{H}(\Omega); \tag{7}$$

$$\text{Find } \gamma_{fa}^{(i)} \in \mathcal{H}(\Omega) \text{ with } \gamma_{fa}^{(i)} = 0 \text{ at } O, \text{ satisfying}$$

$$\int_\Omega r_f^2\nabla\gamma_{fa}^{(i)}\cdot\nabla\tilde{\gamma}_{fa}^{(i)} + \gamma_{fa}^{(i)}\tilde{\gamma}_{fa}^{(i)} - \frac{\partial\bar{\sigma}}{\partial\gamma_p^{(i)}}\frac{\partial\gamma_p^{(i)}}{\partial\gamma_f^{(i)}}\frac{\nabla\bar{z}^{(i)}\cdot\nabla\bar{z}_a^{(i)}}{\sqrt{(L/z_0)^2+\left|\nabla\bar{z}^{(i)}\right|^2}}\tilde{\gamma}_{fa}^{(i)}\,\mathrm{d}\Omega = 0,\ \tilde{\gamma}_{fa}^{(i)} \in \mathcal{H}(\Omega). \tag{8}$$

where $\bar{z}_a^{(i)}$ and $\gamma_{fa}^{(i)}$ are the adjoint variables of $\bar{z}^{(i)}$ and $\gamma_f^{(i)}$, respectively; $\tilde{\bar{z}}_a^{(i)}$ and $\tilde{\gamma}_{fa}^{(i)}$ are the test functions of $\bar{z}_a^{(i)}$ and $\gamma_{fa}^{(i)}$, respectively. The gradient of the duty ratio is found to be

$$\delta f_d^{(i)} = \int_\Omega -\gamma_{fa}^{(i)}\delta\gamma^{(i)}\,\mathrm{d}\Omega \tag{9}$$

where $\delta f_d^{(i)}$ is the first-order variation of the duty ratio $f_d^{(i)}$; $\gamma_{fa}^{(i)}$ is found by solving the weak adjoint equation of the Helmholtz filter:

$$\text{Find } \gamma_{fa}^{(i)} \in \mathcal{H}(\Omega) \text{ with } \gamma_{fa}^{(i)} = 0 \text{ at } O, \text{ satisfying}$$

$$\int_\Omega r_f^2\nabla\gamma_{fa}^{(i)}\cdot\nabla\tilde{\gamma}_{fa}^{(i)} + \gamma_{fa}^{(i)}\tilde{\gamma}_{fa}^{(i)} - S^{(i)}\frac{\partial\gamma_p^{(i)}}{\partial\gamma_f^{(i)}}\tilde{\gamma}_{fa}^{(i)}\,\mathrm{d}\Omega = 0,\ \forall\tilde{\gamma}_{fa}^{(i)} \in \mathcal{H}(\Omega). \tag{10}$$

More details for the adjoint analysis have been provided in Appendix A.3.

2.3. Solving the patterns

The inverse design procedure was implemented as outlined by the pseudo codes in Table 1, where a main loop in Table 1a includes two sub-loops in Table 1b and c, i.e., one for the heuristic bisection procedure used to determine the indicators of the design domains (Table 1b), and the other one for the iterative solution of the variational problem in Eq. (5) (Table 1c). The finite element method is utilized to solve the relevant partial differential equations and corresponding adjoint equations. Triangular elements with maximal size 1/240 are used to discretize the irreducible triangular-domains shown in Fig. 2. The finite element solver can be implemented by choosing a finite element software package which includes a nonlinear solver. In the inverse design procedure, the projection parameter β with initial value 1 is doubled after every 30 iterations, for each layer of the micro-texture; the sub-loop to solve the variational problem in Eq. (5) is stopped when the maximal iteration number is reached, or if the averaged variation of the design objective in continuous 5 iterations and the residual of the duty-ratio constraint are simultaneously less than the specified tolerance 10^{-3}. The design variable is updated using the method of moving asymptotes (MMA) [60].

2.4. Generating the overlayed micro-textures

By the procedure outlined in Table 1, the patterns for all layers of the micro-textures can be obtained. In each instance, they are represented by the physical density in the dimensionless irreducible-triangles. The final patterns for the micro-textures are generated by reflections, scalings, extrusions, and pile-ups of these patterns. Based on such a series of operations, each layer has a quasi three-dimensional configuration with an extruding geometry; the pattern of the current layer is a subset of that of its downward layer; this arrangement is ensured by the indicators of the design domains. Therefore, the micro-textures have overlayed geometry guaranteeing the manufacturability using an overlayed photolithography process [36]. Before generating the overlayed micro-textures based on the computed patterns, a scaling factor and extrusion distance need be determined.

Table 1
(a) Pseudocode for the inverse design of a overlayed micro-texture. In the inner loop for the iterative solution of the variational problem in Eq. (5), n^{sub} is the loop-index, and n_{max}^{sub} is the maximal value of n^{sub}. (b) Pseudocode for a heuristic bisection procedure used to determine the indicators of the design domains. (c) Pseudocode for an iterative solution of the variational problem in Eq. (5), where $J_{n^{sub}}^{(i)}$ is the value of $J^{(i)}$ in the n^{sub}th iteration, and mod is the operator used to take the remainder.

```
(a) Main loop

Choose $\bar{\sigma}_l$, $N$, $\left\{f_0^{(1)}, f_0^{(2)}, \ldots, f_0^{(N)}\right\}$, $\left\{\Delta f_s^{(0)}, \Delta f_s^{(1)}, \ldots, \Delta f_s^{(N-1)}\right\}$ with $\Delta f_s^{(0)} = 0$;
Set $n_{max}^{sub} \leftarrow 327$ and $i \leftarrow 1$;
loop
    Set $\gamma^{(i)} \leftarrow f_0^{(i)}$, $n^{sub} \leftarrow 1$, $\xi \leftarrow 0.5$ and $\beta \leftarrow 1$;
    if $i == 1$,
      $S^{(i)}(\mathbf{x}) = 1$, for $\forall \mathbf{x} \in \Omega$;
    else
      Set $r_{Smax} \leftarrow 1$ and $r_{Smin} \leftarrow 0$;
      sub-loop 1 in Table 1b;
    end(if)
    sub-loop 2 in Table 1c;
    if $i == N$,
      break;
    else $i \leftarrow i + 1$;
    end(if)
end(loop)

(b) Sub-loop 1
sub-loop 1
    Set $r_S \leftarrow (r_{Smax} + r_{Smin})/2$;
    Solve Eq. (19) to derive $S^{(i)}$;
    Compute $S^{(i)}$ from Eq. (20) and calculate $A_E = \int_\Omega S^{(i)} \,\mathrm{d}\Omega$;
    if $\left|\left(A_E - \int_\Omega S^{(i-1)} \gamma_p^{(i-1)} \,\mathrm{d}\Omega\right) - \Delta f_s^{(i-1)}\right| \Big/ \Delta f_s^{(i-1)} \le 1 \times 10^{-3}$,
      break;
    elseif $A_E > \int_\Omega S^{(i-1)} \gamma_p^{(i-1)} \,\mathrm{d}\Omega$,
      $r_{Smax} \leftarrow r_S$;
    else $r_{Smin} \leftarrow r_S$;
    end(if)
end(sub-loop 1)

(c) Sub-loop 2
sub-loop 2
    Derive $\gamma_p^{(i)}$ by filtering and projecting $\gamma^{(i)}$, and compute $f_d^{(i)}$;
    Solve $\bar{z}^{(i)}$ and evaluate $J_{n^{sub}}^{(i)}$;
    Solve $\bar{z}_a^{(i)}$ and $\gamma_{fa}^{(i)}$ from equations 9 and 10, and evaluate $\delta J^{(i)}/J_0$ from equation 8;
    Solve $\gamma_{fa}^{(i)}$ from equation 12, and evaluate $\delta f_d^{(i)}$ from equation 11;
    Update $\gamma^{(i)}$ based on $\delta J^{(i)}/J_0$ and $\delta f_d^{(i)}$;
    if mod $\left(n^{sub}, 30\right) == 0$ and $n^{sub} > 0$
      $\beta \leftarrow 2\beta$;
    end(if)
    if $\left(n^{sub} == n_{max}^{sub}\right)$ or
      $\left(\beta == 2^{10}, \frac{1}{5} \sum_{m=0}^{4} \left|J_{n^{sub}}^{(i)} - J_{n^{sub}-m}^{(i)}\right| \Big/ J_0 \le 10^{-3}, \text{ and } \left|f_d^{(i)} - f_0^{(i)}\right| \le 10^{-3}\right)$
      break;
    end(if)
    $n^{sub} \leftarrow n^{sub} + 1$
    end(sub-loop 2)
```

2.4.1. *Scaling factor*

The scaling factor can be determined based on a scaling property of the pattern, which follows from a solution property of the dimensionless Young–Laplace Eq. (1):

$$\bar{z}_{l_s}^{(i)}(l_s \mathbf{x}) = l_s \bar{z}^{(i)}(\mathbf{x}), \ \forall \mathbf{x} \in \Omega \text{ and } \forall l_s \mathbf{x} \in \Omega_{l_s}. \tag{11}$$

where l_s is the scaling factor, and $\bar{z}_{l_s}^{(i)}$ is the liquid/vapour interface on the scaled domain $\Omega_{l_s} = \left\{\mathbf{x}' : \mathbf{x}' = l_s \mathbf{x}, \forall \mathbf{x} \in \Omega\right\}$, i.e., a solution of the dimensionless Young-Laplace equation defined on Ω_{l_s}. Under the precondition of constant $\bar{\sigma}_l = \sigma_l/(LP)$, with σ_l representing the liquid surface tension, the desired working pressure corresponding to l_s is $P^{(l_s)} = LP/l_s$. Then, a smaller scaling factor will achieve more robust Cassie–Baxter mode. However, the overlayed photolithography process physically fixes the feasible minimum feature size of a pattern. Therefore, a lower bound of the scaling factor corresponds to a manufacturability constraint, and is determined based on a feasible minimum feature size.

On the other hand, because a scaled pattern should retain the dominant role of the surface tension in suspending the liquid, its surface-to-volume ratio should be much larger than one. Hence, the scaling factor should satisfy

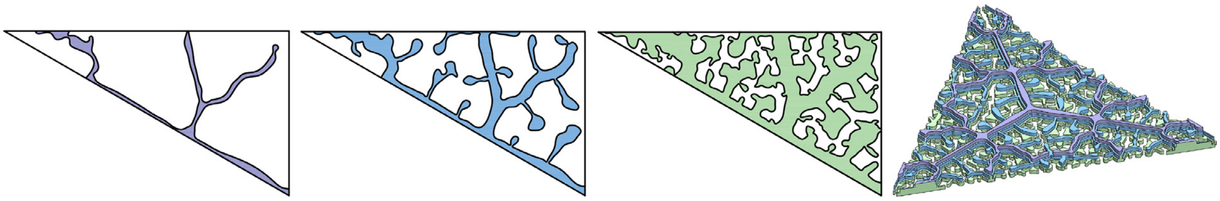

(a) Regular triangle

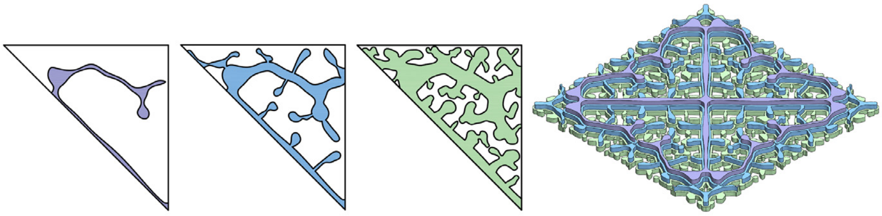

(b) Regular quadrangle

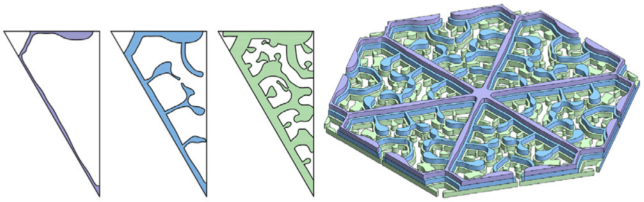

(c) Regular hexagon

Fig. 5. Inversely design patterns corresponding to each layer of a micro-texture. To the right, the micro-textures are assembled into surface patterns.

$$l_s \ll \min_{i\in\{1,2,\ldots,N\}} \frac{S_c^{(i)}}{V_c^{(i)}} \tag{12}$$

where $S_c^{(i)} = \int_\Omega \sqrt{1+|\nabla \bar{z}_c^{(i)}|^2}\,\mathrm{d}\Omega$ and $V_c^{(i)} = |\int_\Omega \bar{z}_c^{(i)}\,\mathrm{d}\Omega|$ are respectively the surface area and bulk volume of the liquid bulges, with $\bar{z}_c^{(i)}$ representing the liquid/vapor interface corresponding to the critical static pressure $P_c^{(i)}$ for the ith layer of the micro-texture. As a performance criterion of the computed micro-texture, the critical static pressure $P_c^{(i)}$ can be determined according to the fact that the maximal value of the contact angle at the sidewalls of the ith layer is not larger than its crucial advancing value, when the three-phase contact lines are anchored at the boundary of the upper level surface of the ith layer:

$$\sup_{\mathbf{x}\in\partial\mathcal{N}^{(i)}\backslash\partial\Omega} \theta^{(i)}(\mathbf{x}) \le \theta_A,\ \ i\in\{1,2,\ldots,N\}. \tag{13}$$

Here, $\mathcal{N}^{(i)} \subset \Omega$ is the null space of $S^{(i)}\gamma_p^{(i)} > 1/2$ at the minimum liquid-bulge measurement of the liquid/vapor interface, i.e.,

$$\mathcal{N}^{(i)} = \begin{cases} \left\{ \mathbf{x}\in\Omega : \left(S^{(i)}\gamma_p^{(i)}\Big|_{\substack{\arg\min J^{(i)} \\ \gamma^{(i)}\in[0,1]}} > \frac{1}{2} \right) \in \{0\} \subset \{0,1\} \right\}, & i\in\{1,2\cdots N\} \\ \Omega, & i\in\{N+1\} \end{cases} \tag{14}$$

and 1/2 is the average of the elements in {0, 1}. The contact angle

$$\theta^{(i)}(\mathbf{x}) = \pi - \cos^{-1}\left(\frac{\nabla \bar{z}^{(i)}}{\left|\nabla \bar{z}^{(i)}\right|} \cdot \mathbf{n}_{\mathcal{N}^{(i)}} \right),\ \ \forall \mathbf{x} \in \partial\mathcal{N}^{(i)}\backslash\partial\Omega \tag{15}$$

is formed at the boundary of the i-th layer, with $\mathbf{n}_{\mathcal{N}^{(i)}}$ representing the outward unit normal at the boundary of $\mathcal{N}^{(i)}$; for micro-textures with known material, θ_A is the critical advancing contact angle, and its value is usually found from experimental tests. Notably, θ_A is equal to its equilibrium counterpart, when the sidewalls are regarded to be smooth and chemically homogeneous; otherwise, it is larger in the hydrophobic case.

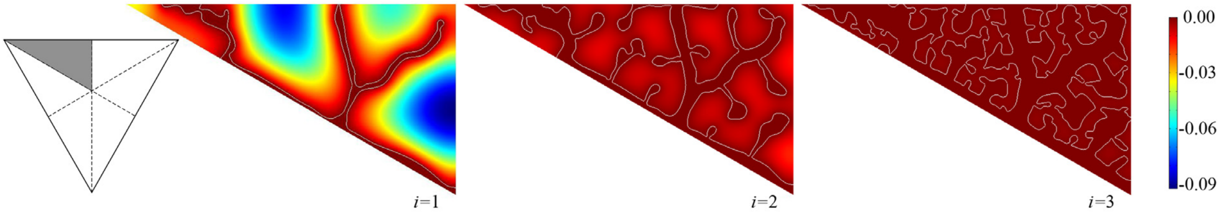

(a) Regular triangle

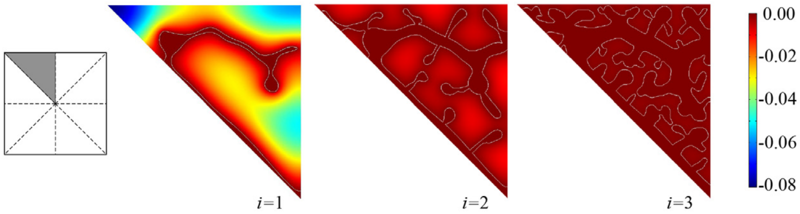

(b) Regular quadrangle

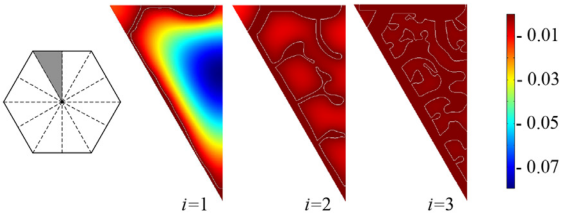

(c) Regular hexagon

Fig. 6. Computed distribution of the normalized vertical coordinate of the liquid/vapor interface supported on the inversely designed micro-textures.

The critical static pressure $P_c^{(i)}$ and the corresponding liquid/vapor interface $\bar{z}_c^{(i)}$ is determined by the heuristic bisection method with an upper bound found by a double procedure, described in Appendix A.4. It can be concluded that the critical static pressure satisfies $P_c^{(1)} < P_c^{(2)} < \cdots < P_c^{(N)}$, because the robustness of the Cassie–Baxter mode progressively increases along with the ceiling-to-floor enlargement of the duty ratio.

After finding the critical static pressures and their corresponding liquid/vapor interfaces, the scaling factor can be evaluated; a reasonable scaling factor finds a compromise between the robustness of the Cassie–Baxter mode and manufacturability of the overlayed micro-textures.

2.4.2. Extrusion distance

The extrusion distance for every layer of the scaled pattern can be large enough to avoid a collapse of the Cassie–Baxter mode. This collapse would be caused by the liquid/vapour interface touching the surface or walls of the micro-texture terraces before the working pressure has reached its critical static value. The extrusion distance of the current layer is commonly determined by that of the higher up layers and the depth suprema of the liquid/vapor interfaces suspended over the difference sets of the current pattern and its downward neighbor terraces. Thus, the extrusion distance $d_e^{(i)} = \frac{l_s}{L} z_0 \bar{d}_e^{(i)}$ of the ith layer should be chosen with $\bar{d}_e^{(i)}$ satisfying the following recursion inequality:

$$\bar{d}_e^{(i)} > \max_{n\in\{1,2\cdots i\}} \left\{ \sup_{\mathbf{x}\in\mathcal{N}^{(i+1)}\setminus\mathcal{N}^{(i)}} \left|\bar{z}_c^{(n)}\right| - \sum_{k=1}^{i-n} \bar{d}_e^{(k)} \right\},\quad i\in\{1,2\cdots N\}, \tag{16}$$

where sup is the supremum operator; $\bar{d}_e^{(i)}$ is the normalized counterpart of the extrusion distance for the scaled patterns. More details on this recursion inequality are provided in Appendix A.5.

Based on the determined scaling factor and extrusion distance, the aspect ratio can be evaluated for the micro-textures, and it is another important index used to characterize the manufacturability. Because the pattern has a dimensionless feature size of the magnitude of the filter radius r_f, the scaled pattern of the ith layer has a feature size of the magnitude of $l_s r_f$. Because the condition

$$\max_{n\in\{1,2\cdots N\}} \left\{ \sup_{\mathbf{x}\in\Omega} \left|\bar{z}_c^{(n)}\right| \right\} > \max_{n\in\{1,2,\ldots,i\}} \left\{ \sup_{\mathbf{x}\in\mathcal{N}^{(i+1)}\setminus\mathcal{N}^{(i)}} \left|\bar{z}_c^{(n)}\right| - \sum_{k=1}^{i-n} \bar{d}_e^{(k)} \right\},\quad i\in\{1,2,\ldots,N\} \tag{17}$$

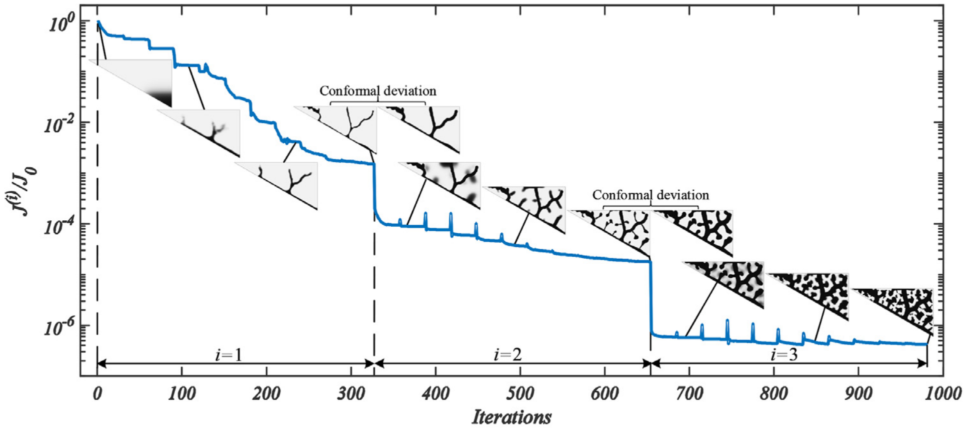

(a) Regular triangle

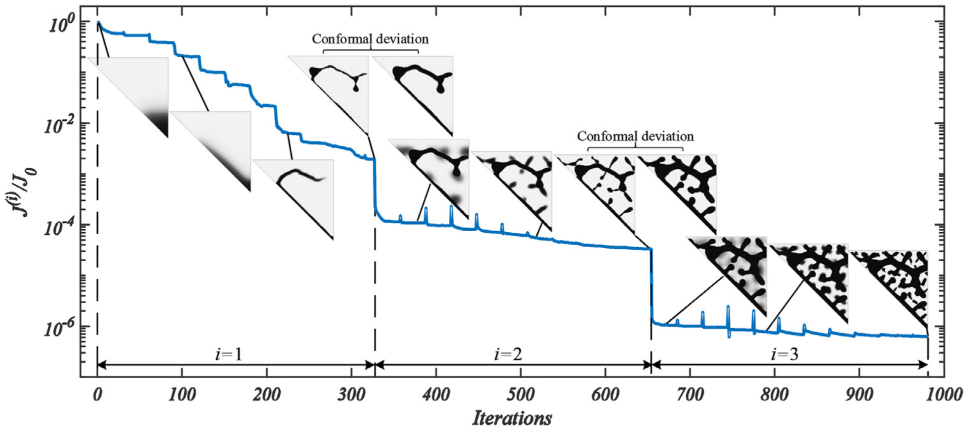

(b) Regular quadrangle

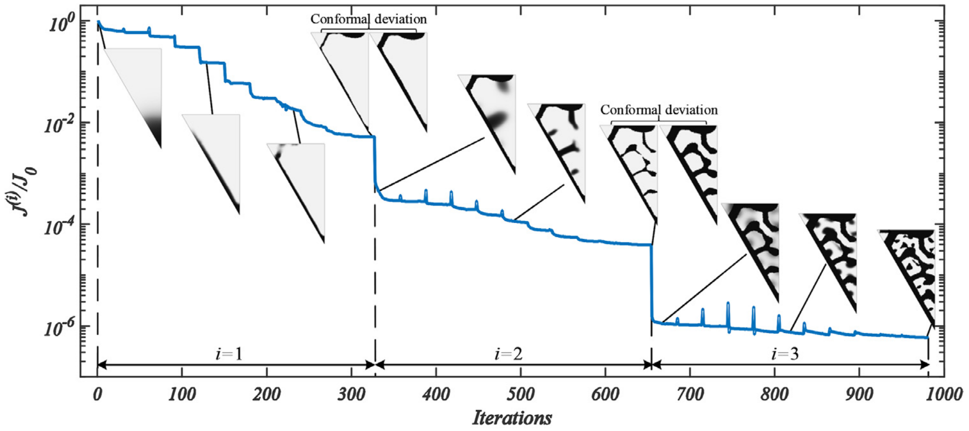

(c) Regular hexagon

Fig. 7. Convergence history of the iterative solution process, corresponding to the designs of Fig. 5. A step downward in the curve correspond to the hierarchy achieved by the conformal deviation. Snapshots of the evolved density topology are shown as inserts; at the downward steps the conformal pattern extension is also illustrated.

is satisfied, the normalized extrusion distance $\bar{d_e}^{(i)}$ can be approximated to be within the magnitude of $\max_{n\in\{1,2\cdots N\}}\{\sup_{\mathbf{x}\in\Omega}|\bar{z}_c^{(n)}|\}$, which in turn is within the magnitude of r_f. Therefore, the aspect ratio of the ith layer of the micro-textures can be approximated as

$$R_a^{(i)} \sim \frac{1}{L} z_0 \bar{d_e}^{(i)} / r_f \sim \frac{1}{L} z_0 < 1, \;\; i \in \{1, 2, \ldots, N\}. \tag{18}$$

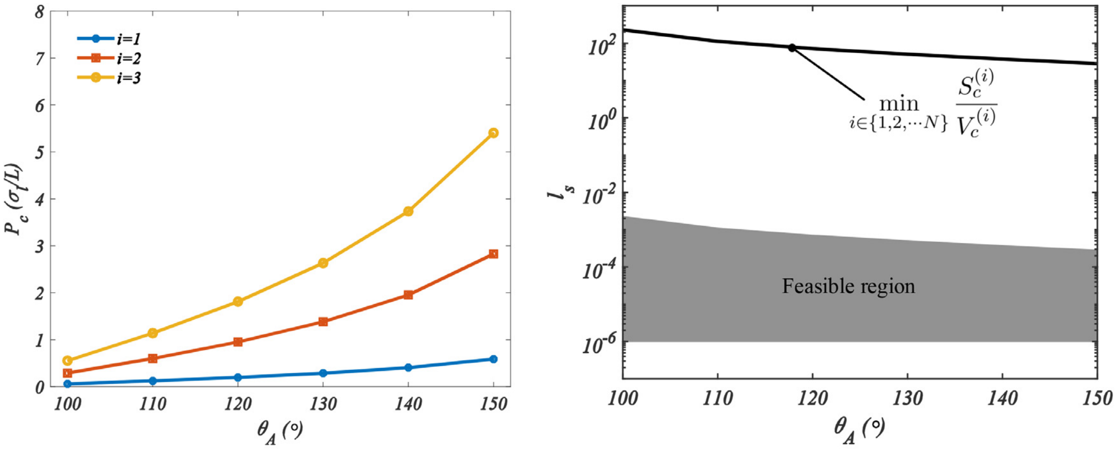

(a) Critical static pressures for regular-triangle case (b) Feasible region for the scaling factor of regular triangle

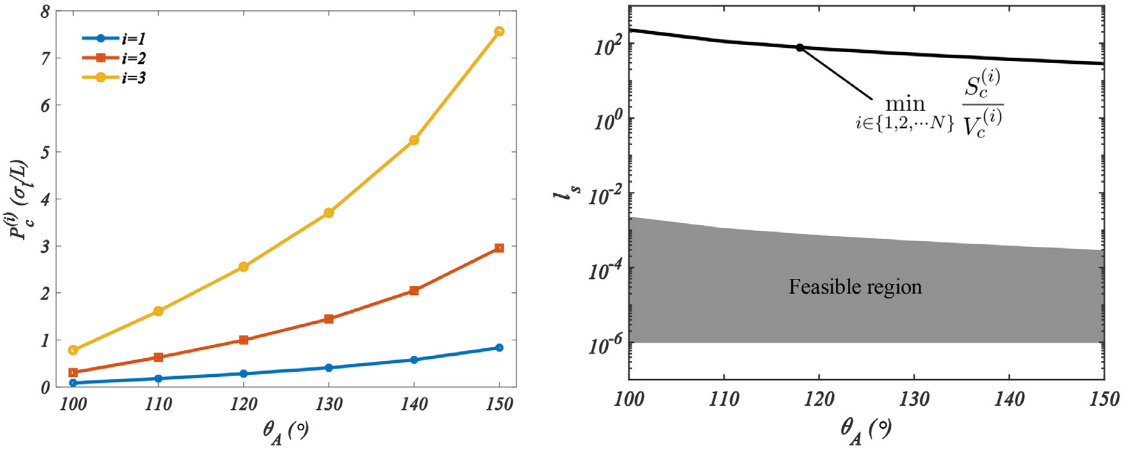

(c) Critical static pressures for regular-quadrangle case (d) Feasible region for the scaling factor of regular quadrangle

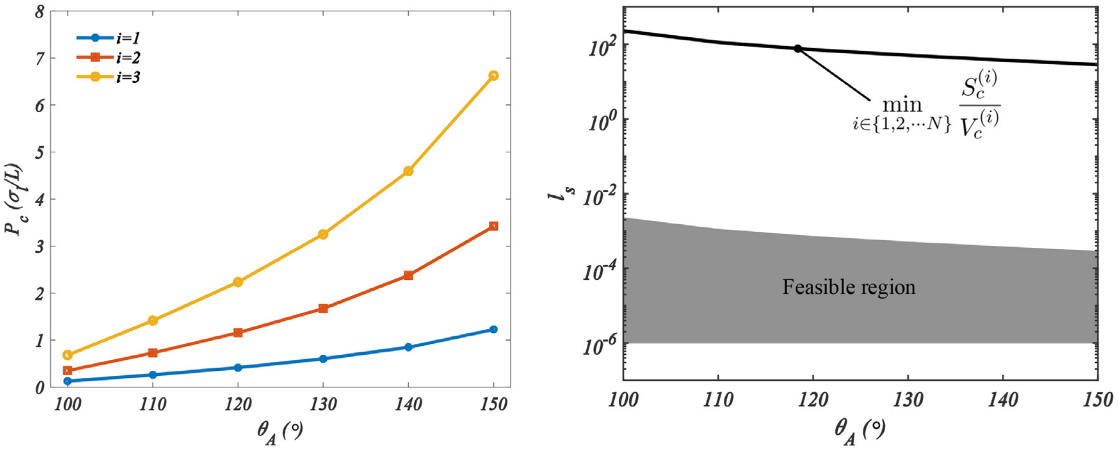

(e) Critical static pressures for regular-hexagon case (f) Feasible region for the scaling factor of regular hexagon

Fig. 8. Plots (a), (c), and (e) show the critical static pressures in the unit of σ_l/L versus different values of the critical advancing contact angle. Plots (b), (d) and (f) describe the feasible regions for the scaling factors. The rows correspond to each of the three tiling patterns.

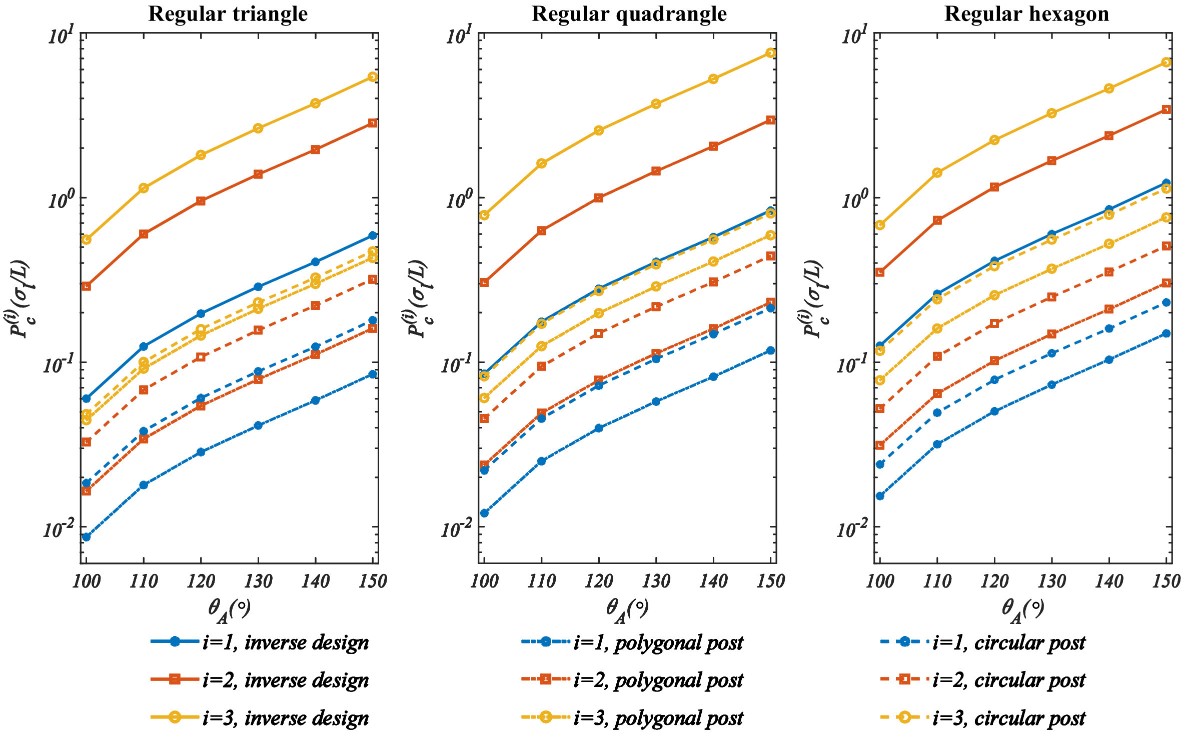

Fig. 9. Plots for the critical static pressures in the unit of σ_l/L versus different values of the critical advancing contact angle, respectively for the derived micro-textures and the ones composed of hierarchical posts with regular-polygonal and circular cross sections.

Table 2
Parameters used for solving the variational problem in Eq. (5).

$\bar{\sigma}_l$	r_f	L	z_0
1	4/120	10 μm	1 μm

From Eq. (18), it can be concluded that an inversely designed overlayed micro-texture features favourable manufacturability from the viewpoint of aspect ratio. The trace height due to this aspect-ratio is a reason for terming the periodic micro-texture as *artificial roughness*.

3. Results and discussion

In this section, the overlayed micro-textures are numerically investigated for their wetting behavior in the Cassie–Baxter mode. Under the manufacturing constraint of overlayed photolithography, the micro-textures with triple layers are inversely designed by the method introduced in Section 2, for which the design parameters are chosen to be

$$N = 3, \left\{ f_0^{(1)} = 0.1, f_0^{(2)} = 0.3, f_0^{(3)} = 0.6 \right\}, \left\{ \Delta f_s^{(0)} = 0, \Delta f_s^{(1)} = 0.1, \Delta f_s^{(2)} = 0.2 \right\},$$

along with those listed in Table 2. For the three types of periodicity demonstrated in Fig. 1, the patterns for each layer of the micro-textures shown in Fig. 5 are obtained by solving the variational problem in Eq. (5). The distributions of the normalized vertical coordinate of the liquid/vapor interfaces supported on the derived patterns are shown in Fig. 6. The convergence histories of the iterative solutions, and corresponding density pattern evolutions, are shown in Fig. 7, which indicates that the convergence is essentially monotonic. Therefore, the robustness of the iterative solution procedure is conformed. In Fig. 7, local jumps and downward steps exist; local jumps are caused by the double operation of the projection parameter β; and downward steps correspond to the liquid-bulge volume decrease along with the duty-ratio increase caused by the conformal extension of the pattern, where the hierarchy is achieved by the conformal deviation.

After the patterns are obtained, the periodic units of the triple-layered micro-textures are generated as shown in Fig. 5, using the procedures demonstrated in Appendix A.1. The scaling factor and extrusion distance should be determined in advance of texture-generation. The critical static pressures are computed for the patterns by the procedure sketched in Appendix A.4. For different critical advancing contact angles, the derived critical static pressures in the unit of σ_l/L are plotted in Fig. 8a, c and e. A range of the advancing contact angle can be targeted through specific choice of materials

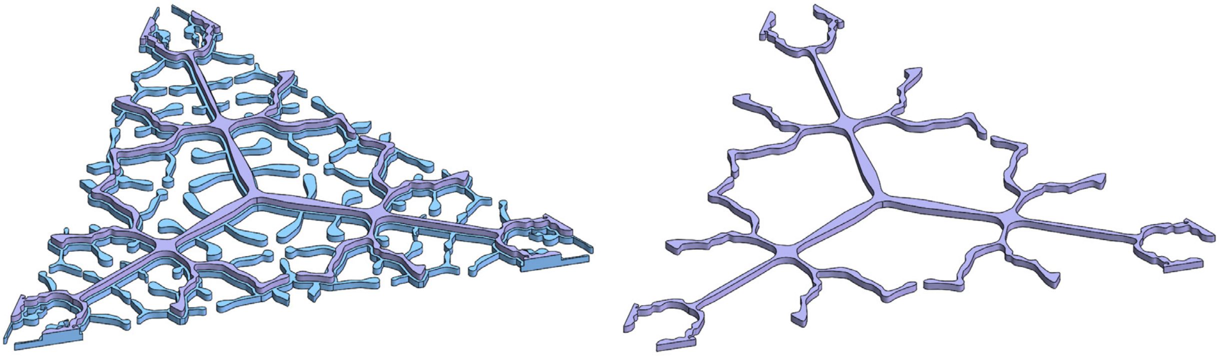
(a) Two-layered regular-triangle unit (b) One-layered regular-triangle unit

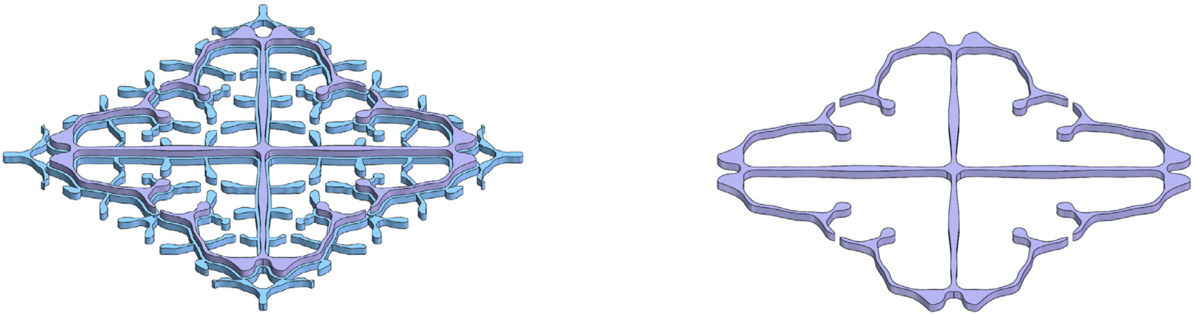
(c) Two-layered regular-quadrangle unit (d) One-layered regular-quadrangle unit

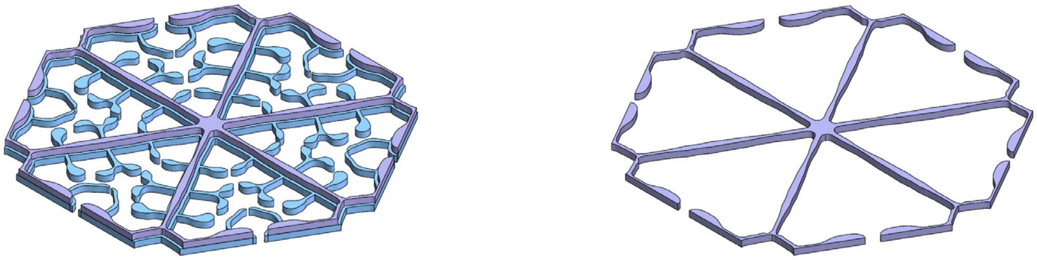
(e) Two-layered regular-hexagon unit (f) One-layered regular-hexagon unit

Fig. 10. Overlayed micro-textures are flexible on enhancing the manufacturability by removing a lower layer to reduce the number of manufacturing steps, with keeping the performance of the remaining layers.

for the micro-textures. It is noted that the critical static pressure of each layer increases in the ceiling-to-floor direction. This corresponds to the improvement in robustness of the Cassie–Baxter mode brought by each additional layer. It can also be concluded that the critical static pressure increases along with an enlargement of the advancing contact angle. This is because that a larger advancing contact angle corresponds to a critical liquid/vapor interface with larger curvature and hence larger critical static pressure. Sequentially, the scaling factor and extrusion distance can be determined based on the geometrical properties of the critical liquid/vapor interface corresponding to a given advancing contact angle.

For the scaling factor, the surface-volume ratios are computed for the critical liquid/vapor interfaces, supported on their corresponding layers of the micro-textures. For each periodic pattern, the minimal surface-volume ratio corresponding to different layers are plotted for a range of advancing contact angles, shown in Fig. 8b, d, and f. To reduce the scaling factor to far below the minimal surface-volume ratio, the upper limit of l_s is set to be 10^{-5}-fold of its corresponding minimal surface-volume ratio. The lower limit is set to be 10^{-6}, corresponding to a lattice constant of 1 µm, which is feasible for an electron-beam lithography process. With these parameters, the scaling factor can be determined in the feasible regions marked in Figure 8b, d, and f.

For the extrusion distance, the recursion inequality in Eq. (16), detailed in Appendix A.5, can be computed based on the depth of the critical liquid/vapor interfaces. As demonstrated by Fig. 8a, c, and e, the depth of the critical liquid/vapor interface increases along with the enlargement of the critical advancing angle, because of the increase of the critical static

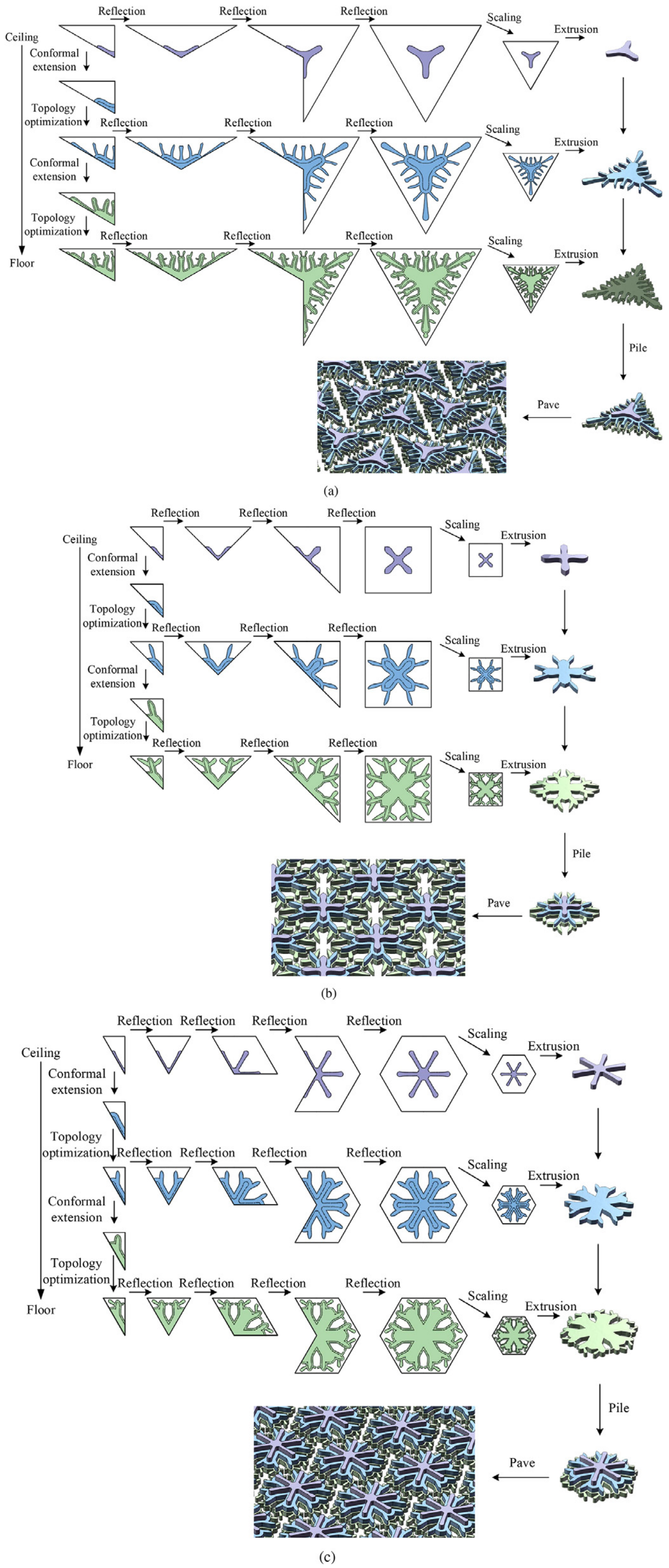

Fig. 11. Sketch of the inverse design procedure for overlayed micro-textures with the regular-triangle (a), regular-quadrangle (b) and regular-hexagon (c) tiling.

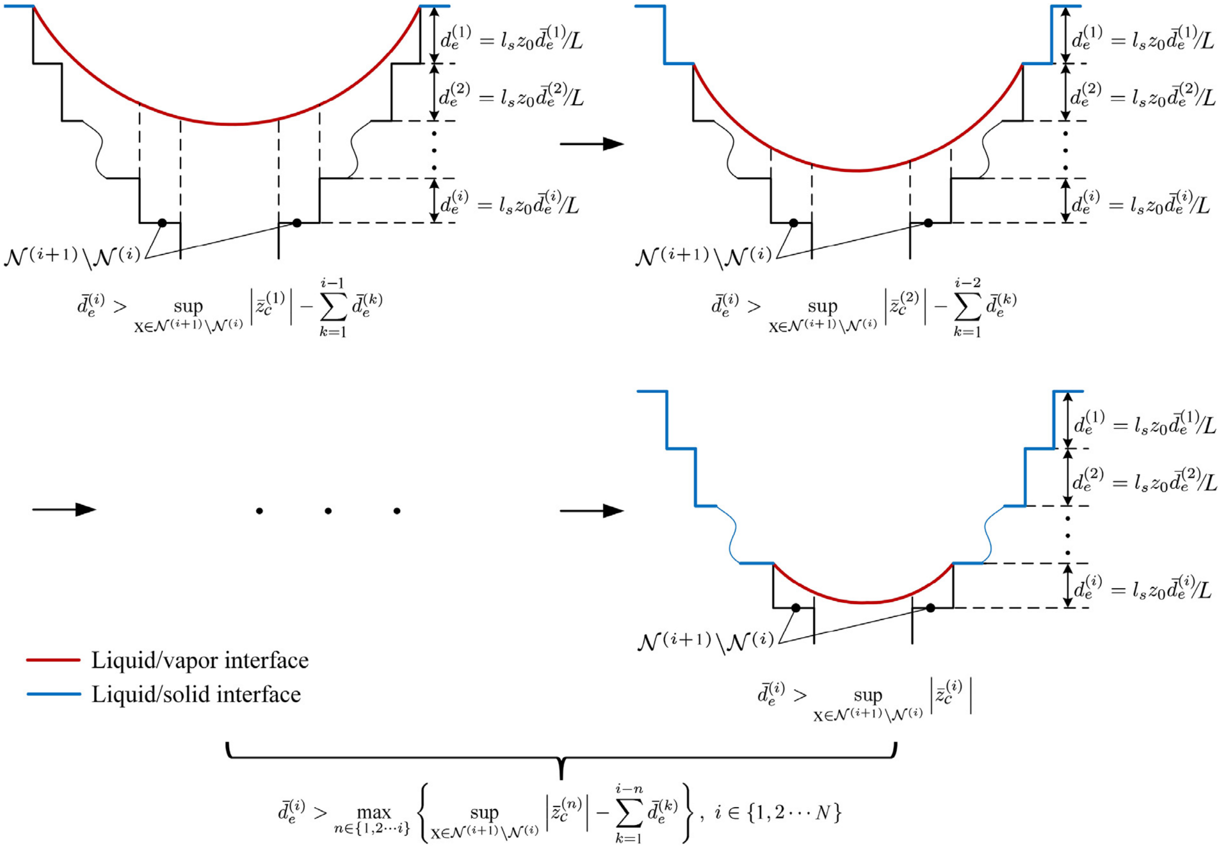

Fig. 12. Profile sketch illustrating the recursion inequality (Eq. (16)) for an extrusion distance of the pattern for the *i*th layer of the micro-texture.

Table 3
Recursion inequalities for the normalized extrusion distance of the derived patterns shown in Fig. 5.

(a) Recursion inequalities for the patterns in Fig. 5a.
$\bar{d}_e^{(1)} > 0.0535$
$\bar{d}_e^{(2)} > \max\left\{0.0404 - \bar{d}_e^{(1)}, 0.0301\right\}$
$\bar{d}_e^{(3)} > \max\left\{0.0542 - \bar{d}_e^{(2)} - \bar{d}_e^{(1)}, 0.0372 - \bar{d}_e^{(1)}, 0.0132\right\}$
(b) Recursion inequalities for the patterns in Fig 5b.
$\bar{d}_e^{(1)} > 0.0656$
$\bar{d}_e^{(2)} > \max\left\{0.0663 - \bar{d}_e^{(1)}, 0.0313\right\}$
$\bar{d}_e^{(3)} > \max\left\{0.0671 - \bar{d}_e^{(2)} - \bar{d}_e^{(1)}, 0.0321 - \bar{d}_e^{(1)}, 0.0135\right\}$
(c) Recursion inequalities for the patterns in Fig 5c.
$\bar{d}_e^{(1)} > 0.0927$
$\bar{d}_e^{(2)} > \max\left\{0.0975 - \bar{d}_e^{(1)}, 0.0394\right\}$
$\bar{d}_e^{(3)} > \max\left\{0.0980 - \bar{d}_e^{(2)} - \bar{d}_e^{(1)}, 0.0413 - \bar{d}_e^{(1)}, 0.0112\right\}$

pressure. Therefore, the critical liquid/vapor interfaces are set to be the ones corresponding to the critical advancing angle 150°. In this case, the derived extrusion distance can ensure that the micro-textures are effective for materials with inherent critical advancing angle smaller than 150°. Furthermore, the extrusion distance, normalized by $\frac{l_s}{L} z_0$, should satisfy the inequalities listed in Table 3, from which we can obtain a set of reasonable choice as

$$\bar{d}_e^{(1)} = 0.100, \bar{d}_e^{(2)} = 0.045, \bar{d}_e^{(3)} = 0.020$$

for all three tiling patterns. Additionally, by choosing the scaling factor to be $l_s = 10^{-5}$ localized in all the feasible regions marked in Fig. 8b, d, and f, the extrusion distance of the derived patterns are confirmed to be $d_e^{(1)} = 100\,\text{nm}, d_e^{(2)} = 45\,\text{nm}$, and $d_e^{(3)} = 20\,\text{nm}$, for the tiling patterns with lattice size 10 μm.

To confirm the optimality of the derived patterns, and hence the improved performance of the corresponding micro-textures, liquid-bulge measurement values of the liquid/vapour interfaces (Fig. 6) are compared to the interfaces supported

Table 4
Liquid-bulge measurement values of the liquid/vapor interface supported on the derived micro-textures, the micro-textures in [32], and the ones composed of hierarchical posts with regular polygonal and circular cross sections. The optimal entries for the derived micro-textures are noted in bold.

(a) Regular triangle

	Inverse design	Pattern in [32]	Triangular post	Circular post
$i = 1$	$\mathbf{1.48 \times 10^{-3}}$	1.77×10^{-3}	1.68×10^{0}	2.90×10^{0}
$i = 2$	$\mathbf{1.72 \times 10^{-5}}$	1.13×10^{-4}	1.10×10^{-1}	3.68×10^{-1}
$i = 3$	$\mathbf{3.23 \times 10^{-7}}$	3.51×10^{-6}	1.90×10^{-3}	6.41×10^{-2}

(b) Regular quadrangle

	Inverse design	Pattern in [32]	Quadrangular post	Circular post
$i = 1$	$\mathbf{8.25 \times 10^{-4}}$	1.05×10^{-3}	9.56×10^{-1}	1.16×10^{0}
$i = 2$	$\mathbf{1.41 \times 10^{-5}}$	9.51×10^{-5}	6.41×10^{-2}	9.22×10^{-2}
$i = 3$	$\mathbf{1.99 \times 10^{-7}}$	2.05×10^{-6}	1.35×10^{-3}	5.77×10^{-3}

(c) Regular hexagon

	Inverse design	Pattern in [32]	Hexagonal post	Circular post
$i = 1$	$\mathbf{1.60 \times 10^{-3}}$	1.67×10^{-3}	7.29×10^{-1}	7.80×10^{-1}
$i = 2$	$\mathbf{1.27 \times 10^{-5}}$	8.23×10^{-5}	5.11×10^{-2}	5.61×10^{-2}
$i = 3$	$\mathbf{1.77 \times 10^{-7}}$	1.15×10^{-6}	1.17×10^{-3}	1.61×10^{-3}

by the other micro-textures, as listed in Table 4; the compared micro-textures include the ones with the patterns in [32] (inversely designed by fixing corresponding polygonal parts with the duty ratio 3×10^{-2}) and their conformal extension respectively for the first and downward layers, and the ones composed of hierarchical posts with regular polygonal and circular cross sections, where the duty ratios are kept to be the same as the corresponding layers of the current micro-textures. The comparison shows that the inversely designed micro-textures achieve flatter liquid/vapour interfaces, with effective reduction of the liquid-bulge measurement. The improved robustness of the inversely designed micro-textures are demonstrated through their enhancement of the critical static pressure. Compared to those of the hierarchical posts for different values of critical advancing angle, as shown in Fig. 9, the critical static pressure is enhanced up to 17.7-, 12.9- and 11.3-fold, respectively for the regular triangle, quadrangle, and hexagon tiling patterns.

Because the number of layers of a micro-texture affects the complexity of manufacturing by a lithography process, it is notable that the overlayed micro-textures offer the flexibility to enhance feasibility by dropping lower layers from a particular design without negative effect on the performance of the remaining layers (Fig. 10).

The equilibrium contact angle is a global parameter used to characterize the wetting behavior on a solid surface with micro-textures. When the unit cell of a overlayed micro-texture is embedded periodically in an array, an increase in the equilibrium contact angle is accompanied by an attenuation effect for perturbations to the contact angle, for those cases where the solid surface is micro-textured by a unit-cell array with a fixed repeat size and wetting is in the Cassie–Baxter status [61]. This attenuation effect increases along with a decrease in the ratio of the lattice constant to array size. The micro-textured surface become “slippery”, because the attenuation effect weakens the contact angle hysteresis, an important phenomenon in wetting behavior [61,62]. By logical extension, an overlayed micro-texture with relatively small length scale can reduce the contact angle hysteresis.

4. Conclusions

This article presented a monolithic inverse design approach aimed at achieving improved robustness of Cassie–Baxter mode for the wettability of solid surfaces. The micro-textures are in overlayed geometry with manufacturability for an overlayed lithography process. The inverse design approach is composed of a series of sequentially implemented topology optimizations, with each cycle delivering the pattern of the subsequent layer. The topology optimization is implemented for three dimensionless irreducible triangles, derived from the symmetry of three regular polygons (triangle, quadrangle, hexagon) used to tile a flat surface. The Cassie–Baxter status is described by a dimensionless Young–Laplace equation. It has been demonstrated conclusively that the procedure works properly and is able to achieve a design with the desired wetting performance.

Because the designed structures are able to minimize the perturbation of the liquid surface topology from the flat, whilst simultaneously minimizing the contact area with the solid wall, a number of advantageous properties emerge that may have important consequences for applications. The pattern’s relative height above the surface remains of low profile, making it less prone to damage. The gain in effective contact angle relative to what is possible with the constituent material’s inherent surface energy makes this a potentially graded or variable and tunable surface feature, for example through the use of adaptive/switchable materials to form the patterns. The potentially achieved low contact angle hysteresis will have consequences for fluid-structure interaction, as well as tangential drag and super-icephobic surfaces, which may be useful in protecting equipments and regulating fluids. For other environments, decoupling wetting behaviour from molecular composition frees up the material to focus on further aspects in the flow environment, such as fouling and chemical resistance. In the future, we will address these issues, through exploration of the micro-/nano-fabrication of the overlayed micro-textures and testing the surface-liquid interaction.

Acknowledgments

During this research, Y. Deng acknowledgements a Humboldt Research Fellowship for Experienced Researchers (Humboldt-ID: 1197305), the support from the National Natural Science Foundation of China (No. 51875545), the Youth Innovation Promotion Association of the Chinese Academy of Sciences (No. 2018253) and the Open Fund of SKLAO; Y. Deng also acknowledgements the valuable discussion provided by Yuan Ji from CIOMP and Teng Zhou from Hainan University, during the revision of this manuscript; Z. Liu was supported by the National Natural Science Foundation of China (No. 51675506); J.G. Korvink acknowledges support from an EU2020 FET grant (TiSuMR, 737043), the DFG under grant KO 1883/20-1 Metacoils, in the framework of the German Excellence Intitiative under grant EXC 2082 "3D Matter Made to Order", and by the VirtMat initiative "Virtual Materials Design". The authors are grateful to Prof. K. Svanberg for supplying the MMA codes. They are also grateful to the editors and reviewers for their kind attention and valuable suggestions.

Appendix A

A.1. Demonstration for the generation procedure of the overlayed micro-textures.

The generation procedure for the micro-textures is demonstrated by the triple-layer cases as sketched in Fig. 11 for three types of tiling.

A.2. Heuristic bisection-procedure used to determine indicator for the design domain.

The indicator for the design domain is determined by the following heuristic bisection-procedure for the ceiling's downward layers:

1. Set the upper and lower bounds of an extention radius r_S to be $r_{Smax} = 1$ and $r_{Smin} = 0$, where the extention radius is used to relax $S^{(i-1)}\gamma_p^{(i-1)}$ by an extension equation expressed as

$$\begin{cases} -\nabla \cdot \left(r_S^2 \nabla S^{(i)} \right) + S^{(i)} = S^{(i-1)}\gamma_p^{(i-1)}, \text{ in } \Omega \\ -r_S^2 \nabla S^{(i)} \cdot \mathbf{n} = 0, \text{ on } \partial\Omega \\ S^{(i)} = 0, \text{ at } O \end{cases} \tag{19}$$

2. Set $r_S = (r_{Smax} + r_{Smin})/2$ and derive $S^{(i)}$ by numerically solving the extension equation 19, further compute $A_E = \int_\Omega S^{(i)} \,\mathrm{d}\Omega$, where

$$S^{(i)} = \frac{\tanh\left(2^{10} \cdot 0.98\right) + \tanh\left(2^{10}\left(S^{(i)} - 0.98\right)\right)}{\tanh\left(2^{10} \cdot 0.98\right) + \tanh\left(2^{10} \cdot (1 - 0.98)\right)}; \tag{20}$$

3. If $|(A_E - \int_\Omega S^{(i-1)}\gamma_p^{(i-1)} \,\mathrm{d}\Omega) - \Delta f_s^{(i-1)}|/\Delta f_s^{(i-1)} \leq 10^{-3}$ is not satisfied, r_{Smax} will be updated to be r_S in the case of $A_E > \int_\Omega S^{(i-1)}\gamma_p^{(i-1)} \,\mathrm{d}\Omega$, r_{Smin} will be updated to be r_S in the case of $A_E \leq \int_\Omega S^{(i-1)}\gamma_p^{(i-1)} \,\mathrm{d}\Omega$, and the heuristic bisection-procedure will return to Step 2; or else, the heuristic bisection-procedure will be stopped after computing the desired indicator $S^{(i)}$.

This heuristic procedure, with pseudocode in Table 1b, is a loop operation, which sequentially relaxes and projects $S^{(i-1)}\gamma_p^{(i-1)}$ to find an extension $S^{(i)}$ with a preset duty-ratio enlargement $\Delta f_s^{(i-1)}$.

A.3. Lagrangian multiplier-based adjoint analysis.

According to the Lagrangian multiplier-based adjoint method [59], the augmented Lagrangian of the variational problem for the topology optimization of the ith layer of the micro-texture is

$$\hat{J}^{(i)} = \int_\Omega \frac{1}{|\Omega|} \bar{z}^{(i)^2} - \bar{\sigma} \frac{\nabla \bar{z}^{(i)} \cdot \nabla \bar{z}_a^{(i)}}{\sqrt{(L/z_0)^2 + \left|\nabla \bar{z}^{(i)}\right|^2}} + r_f^2 \nabla \gamma_f^{(i)} \cdot \nabla \gamma_{fa}^{(i)} + \gamma_f^{(i)} \gamma_{fa}^{(i)} - \gamma^{(i)} \gamma_{fa}^{(i)} \,\mathrm{d}\Omega \tag{21}$$

Table 5
Pseudocode for the heuristic bisection procedure used to determine the critical static pressure $P_c^{(i)}$ for the ith layer of a micro-texture. A double procedure is included to find a reasonable upper bound $P_{max}^{(i)}$.

```
Set $i \leftarrow 1$;
loop
   Choose the initial values of $P_{min}^{(i)} = 0$ and $P_{max}^{(i)}$;
   sub-loop 1 Double procedure used to find a reasonable $P_{max}^{(i)}$:
      Set $P_c^{(i)} \leftarrow P_{max}^{(i)}$;
      Solve Eq. (25) to derive $\bar{z}_c^{(i)}$ and compute $\sup_{\mathbf{x} \in \partial\mathcal{N}^{(i)} \setminus \partial\Omega} \theta^{(i)}\big|_{\bar{z}^{(i)}=\bar{z}_c^{(i)}}$;
      if $\sup_{\mathbf{x} \in \partial\mathcal{N}^{(i)} \setminus \partial\Omega} \theta^{(i)}\big|_{\bar{z}^{(i)}=\bar{z}_c^{(i)}} > \theta_A$;
         break;
      else $P_{max}^{(i)} \leftarrow 2P_c^{(i)}$;
      end(if)
   end(sub-loop 1)
   sub-loop 2 Bisection procedure used to determine $P_c^{(i)}$:
      Set $P_c^{(i)} \leftarrow \left(P_{min}^{(i)} + P_{max}^{(i)}\right) \Big/ 2$;
      Solve Eq. (25) to derive $\bar{z}_c^{(i)}$ and compute $\sup_{\mathbf{x} \in \partial\mathcal{N}^{(i)} \setminus \partial\Omega} \theta^{(i)}\big|_{\bar{z}^{(i)}=\bar{z}_c^{(i)}}$;
      if $0 \le \left(\theta_A - \sup_{\mathbf{x} \in \partial\mathcal{N}^{(i)} \setminus \partial\Omega} \theta^{(i)}\big|_{\bar{z}^{(i)}=\bar{z}_c^{(i)}}\right) \Big/ \theta_A \le 10^{-3}$,
         break;
      elseif $\sup_{\mathbf{x} \in \partial\mathcal{N}^{(i)} \setminus \partial\Omega} \theta^{(i)}\big|_{\bar{z}^{(i)}=\bar{z}_c^{(i)}} \le \theta_A$,
         $P_{min}^{(i)} \leftarrow P_c^{(i)}$;
      else $P_{max}^{(i)} \leftarrow P_c^{(i)}$;
      end(if)
   end(sub-loop 2)
   if $i == N$,
      break;
   else $i \leftarrow i + 1$;
   end(if)
end(loop)
```

where $\bar{z}_a^{(i)}$ is the adjoint variable of $\bar{z}^{(i)}$ with $\bar{z}_a^{(i)} = 0$ at O; $\gamma_{fa}^{(i)}$ is the adjoint variable of $\gamma_f^{(i)}$ with $\gamma_{fa}^{(i)} = 0$ at O. The first order variational of the augmented Lagrangian to the field variable and design variable is

$$\begin{aligned}\delta\hat{J}^{(i)} = \int_\Omega & \frac{2}{|\Omega|}\bar{z}^{(i)}\delta\bar{z}^{(i)} - \bar{\sigma}\frac{\nabla\delta\bar{z}^{(i)} \cdot \nabla\bar{z}_a^{(i)}}{\sqrt{(L/z_0)^2 + \left|\nabla\bar{z}^{(i)}\right|^2}} + \bar{\sigma}\frac{\left(\nabla\bar{z}^{(i)} \cdot \nabla\bar{z}_a^{(i)}\right)\left(\nabla\delta\bar{z}^{(i)} \cdot \nabla\bar{z}^{(i)}\right)}{\left(\sqrt{(L/z_0)^2 + \left|\nabla\bar{z}^{(i)}\right|^2}\right)^3} \\ & - \frac{\partial\bar{\sigma}}{\partial\gamma_p^{(i)}}\frac{\partial\gamma_p^{(i)}}{\partial\gamma_f^{(i)}}\frac{\nabla\bar{z}^{(i)} \cdot \nabla\bar{z}_a^{(i)}}{\sqrt{(L/z_0)^2 + \left|\nabla\bar{z}^{(i)}\right|^2}}\delta\gamma_f^{(i)} + r_f^2\nabla\delta\gamma_f^{(i)} \cdot \nabla\gamma_{fa}^{(i)} + \delta\gamma_f^{(i)}\gamma_{fa}^{(i)} - \delta\gamma^{(i)}\gamma_{fa}^{(i)}\,\mathrm{d}\Omega\end{aligned} \tag{22}$$

where $\delta\bar{z}^{(i)}$, $\delta\gamma_f^{(i)}$ and $\delta\gamma^{(i)}$ are the first order variational of $\bar{z}^{(i)}$, $\gamma_f^{(i)}$ and $\gamma^{(i)}$, respectively. From the Kurash–Kuhn–Tucker condition of the partial differential equation constrained optimization problem [59], the first order variational of the augmented Lagrangian to the field variables satisfies

$$\int_\Omega \frac{2}{|\Omega|}\bar{z}^{(i)}\delta\bar{z}^{(i)} - \bar{\sigma}\frac{\nabla\delta\bar{z}^{(i)} \cdot \nabla\bar{z}_a^{(i)}}{\sqrt{(L/z_0)^2 + \left|\nabla\bar{z}^{(i)}\right|^2}} + \bar{\sigma}\frac{\left(\nabla\bar{z}^{(i)} \cdot \nabla\bar{z}_a^{(i)}\right)\left(\nabla\delta\bar{z}^{(i)} \cdot \nabla\bar{z}^{(i)}\right)}{\left(\sqrt{(L/z_0)^2 + \left|\nabla\bar{z}^{(i)}\right|^2}\right)^3}\,\mathrm{d}\Omega = 0 \tag{23}$$

$$\int_\Omega r_f^2\nabla\delta\gamma_f^{(i)} \cdot \nabla\gamma_{fa}^{(i)} + \delta\gamma_f^{(i)}\gamma_{fa}^{(i)} - \frac{\partial\bar{\sigma}}{\partial\gamma_p^{(i)}}\frac{\partial\gamma_p^{(i)}}{\partial\gamma_f^{(i)}}\frac{\nabla\bar{z}^{(i)} \cdot \nabla\bar{z}_a^{(i)}}{\sqrt{(L/z_0)^2 + \left|\nabla\bar{z}^{(i)}\right|^2}}\delta\gamma_f^{(i)}\,\mathrm{d}\Omega = 0 \tag{24}$$

Without losing the arbitrariness of $\delta\bar{z}^{(i)}$ and $\delta\gamma_f^{(i)}$, one can set $\delta\bar{z}^{(i)} = \tilde{\bar{z}}_a^{(i)}$ with $\forall\tilde{\bar{z}}_a^{(i)} \in \mathcal{H}(\Omega)$ and $\delta\gamma_f^{(i)} = \tilde{\gamma}_{fa}^{(i)}$ with $\forall\tilde{\bar{z}}_a^{(i)} \in \mathcal{H}(\Omega)$, and derive the adjoint system in Eq. (7) and (8), where $\mathcal{H}(\Omega)$ is the first order Hilbert functional space defined on Ω. The adjoint gradient of the variational problem can be derived to be the first order variational of the augmented Lagrangian to the design variable (Eq. (6)). Based on a similar procedure, the adjoint analysis can be implemented for the duty ratio in Eq. (5), thereby deriving the adjoint gradient (Eq. (9)) and the adjoint equation (Eq. (10)).

A.4. Heuristic bisection method used to determine the critical static pressure $P_c^{(i)}$ and its corresponding liquid/vapor interface $\bar{z}_c^{(i)}$.

The critical static pressure $P_c^{(i)}$ and the corresponding liquid/vapor interface $\bar{z}_c^{(i)}$ are determined by a heuristic bisection method with an upper bound found by a double procedure:

1. Set the initial values $P_{min}^{(i)} = 0$ and $P_{max}^{(i)}$ for the lower and upper bonds of $P_c^{(i)}$;
2. Set $P_c^{(i)} = P_{max}^{(i)}$, and compute $\sup_{\mathbf{x}\in\partial\mathcal{N}^{(i)}\backslash\partial\Omega} \theta^{(i)}\big|_{\bar{z}^{(i)}=\bar{z}_c^{(i)}}$, where $\bar{z}_c^{(i)}$ corresponds to the current $P_c^{(i)}$ and is found by solving the following equation:

$$\begin{cases} \nabla\cdot\left(\frac{\sigma}{l_s P_c^{(i)}}\frac{\nabla\bar{z}_c^{(i)}}{\sqrt{(l_s/z_0)^2+\left|\nabla\bar{z}_c^{(i)}\right|^2}}\right) = 1, \ \text{in } \Omega\backslash\mathcal{N}^{(i)} \\ \bar{z}_c^{(i)} = 0, \ \text{in } \mathcal{N}^{(i)} \\ \frac{\sigma}{l_s P_c^{(i)}}\frac{\nabla\bar{z}_c^{(i)}}{\sqrt{(l_s/z_0)^2+\left|\nabla\bar{z}_c^{(i)}\right|^2}}\cdot\mathbf{n} = 0, \ \text{on } \partial\Omega \\ \bar{z}_c^{(i)} = 0, \ \text{at } O \end{cases}; \tag{25}$$

3. if $\sup_{\mathbf{x}\in\partial\mathcal{N}^{(i)}\backslash\partial\Omega} \theta^{(i)}|_{\bar{z}^{(i)}=\bar{z}_c^{(i)}} > \theta_A$ is not satisfied, $P_{max}^{(i)}$ will be updated to be $2P_c^{(i)}$, and the procedure will return to Step 2; else, it will continue to the next step;
4. Set $P_c^{(i)} = (P_{min}^{(i)} + P_{max}^{(i)})/2$, and compute $\sup_{\mathbf{x}\in\partial\mathcal{N}^{(i)}\backslash\partial\Omega} \theta^{(i)}|_{\bar{z}^{(i)}=\bar{z}_c^{(i)}}$, with $\bar{z}_c^{(i)}$ by solving Eq. (25);
5. If $0 \le (\theta_A - \sup_{\mathbf{x}\in\partial\mathcal{N}^{(i)}\backslash\partial\Omega} \theta^{(i)}|_{\bar{z}^{(i)}=\bar{z}_c^{(i)}})/\theta_A \le 10^{-3}$ is not satisfied, $P_{min}^{(i)}$ will be updated to be $P_c^{(i)}$ in the case of $\sup_{\mathbf{x}\in\partial\mathcal{N}^{(i)}\backslash\partial\Omega} \theta^{(i)}|_{\bar{z}^{(i)}=\bar{z}_c^{(i)}} \le \theta_A$, $P_{max}^{(i)}$ will be updated to be $P_c^{(i)}$ in the case of $\sup_{\mathbf{x}\in\partial\mathcal{N}^{(i)}\backslash\partial\Omega} \theta^{(i)}|_{\bar{z}^{(i)}=\bar{z}_c^{(i)}} > \theta_A$, and the bisection procedure will return to Step 4; else, the heuristic bisection procedure will be stopped, delivering the desired $P_c^{(i)}$ and its corresponding $\bar{z}_c^{(i)}$.

The above heuristic bisection procedure can be implemented by the pseudocode in Table 5, determining the critical static pressure for each layer of the micro-texture.

A.5. Details for the recursion inequality in Eq. (16).

For the recursion inequality in Eq. (16), the term $\max_{n\in\{1,2\cdots i\}}\{\sup_{\mathbf{x}\in\mathcal{N}^{(i+1)}\backslash\mathcal{N}^{(i)}} |\bar{z}_c^{(n)}| - \sum_{k=1}^{i-n} \bar{d}_e^{(k)}\}$ is the abstract form of

$$\max\left\{\sup_{\mathbf{x}\in\mathcal{N}^{(i+1)}\backslash\mathcal{N}^{(i)}}\left|\bar{z}_c^{(1)}\right| - \sum_{k=1}^{i-1}\bar{d}_e^{(k)}, \ \sup_{\mathbf{x}\in\mathcal{N}^{(i+1)}\backslash\mathcal{N}^{(i)}}\left|\bar{z}_c^{(2)}\right| - \sum_{k=1}^{i-2}\bar{d}_e^{(k)}, \ \cdots \ \sup_{\mathbf{x}\in\mathcal{N}^{(i+1)}\backslash\mathcal{N}^{(i)}}\left|\bar{z}_c^{(n)}\right| - \sum_{k=1}^{i-n}\bar{d}_e^{(k)}, \right.$$
$$\left. \cdots \ \sup_{\mathbf{x}\in\mathcal{N}^{(i+1)}\backslash\mathcal{N}^{(i)}}\left|\bar{z}_c^{(i-1)}\right| - \bar{d}_e^{(1)}, \ \sup_{\mathbf{x}\in\mathcal{N}^{(i+1)}\backslash\mathcal{N}^{(i)}}\left|\bar{z}_c^{(i)}\right|\right\}. \tag{26}$$

This recursion inequality can be physically and geometrically demonstrated by Fig. 12.

References

[1] X. Feng, L. Jiang, Design and creation of superwetting/antiwetting surfaces, Adv. Mater. 18 (2006) 3063–3078.
[2] R.N. Wenzel, Resistance of solid surfaces to wetting by water, Ind. Eng. Chem. 28 (8) (1936) 988–994.
[3] A.B.D. Cassie, S. Baxter, Wettability of porous surfaces, Trans. Faraday Soc. 40 (1944) 546–551.
[4] J. Bico, C. Marzolin, D. Quéré, Pearl drops, Europhys. Lett. 47 (1999) 220–226.
[5] A. Lafuma, D. Quéré, Superhydrophobic states, Nat. Mater. 2 (2003) 457–460.
[6] L. Scholtès, B. Chareyre, F. Nicot, F. Darve, Micromechanics of granular materials with capillary effects, Int. J. Eng. Sci. 47 (2009) 64–75.
[7] D. Öner, T.J. McCarthy, Ultrahydrophobic Surfaces. Effects of Topography Length Scales on Wettability, Langmuir 16 (2000) 7777–7782.
[8] Q.J. Wang, Y.W. Chung, Encyclopedia of Tribology, Springer, US, 2013.
[9] M. Nosonovsky, Slippery when wetted, Nature 477 (2011) 412–413.
[10] S.A. Zhou, On forces in microelectromechanical systems, Int. J. Eng. Sci. 41 (2003) 313–335.
[11] G. Jenkins, C.D. Mansfield, Microfluidic Diagnostics, Humana Press, 2013.
[12] J. Li, Y. Wei, Z. Huang, F. Wang, X. Yan, Z. Wu, Electrohydrodynamic behavior of water droplets on a horizontal super hydrophobic surface and its self-cleaning application, Appl. Surf. Sci. 403 (2017) 133–140.
[13] L. Feng, Z. Zhang, Z. Mai, Y. Ma, B. Liu, L. Jiang, D. Zhu, A super-hydrophobic and super-oleophilic coating mesh film for the separation of oil and water, Angew. Chem. Int. Ed. 43 (2004) 2012–2014.
[14] M.N. Kavalenka, F. Vüllers, J. Kumberg, C. Zeiger, V. Trouillet, S. Stein, T.T. Ava, C. Li, M. Worgull, H. Hölscher, Adaptable bioinspired special wetting surface for multifunctional oil/water separation, Sci. Rep. 7 (2017) 39970. EP
[15] P. Ragesh, V.A. Ganesh, S.V. Nair, A.S. Nair, A review on 'self-cleaning and multifunctional materials', J. Mater. Chem. A 2 (2014) 14773–14797.
[16] M. Reyssat, A. Pépin, F. Marty, Y. Chen, D. Quéré, Bouncing transitions on microtextured materials, Europhys. Lett. 74 (2006) 306–312.
[17] P. Ragesh, V.A. Ganesh, S.V. Nair, A.S. Nair, Condensation on ultrahydrophobic surfaces and its effect on droplet mobility: ultrahydrophobic surfaces are not always water repellant, Langmuir 22 (2006) 2433–2436.
[18] G. McHale, N.J. Shirtcliffe, M.I. Newton, Contact-angle hysteresis on super-hydrophobic surfaces, Langmuir 20 (2004) 10146–10149.

[19] W. Lee, M.K. Jin, W.C. Yoo, J.K. Lee, Nanostructuring of a polymeric substrate with well-defined nanometer-scale topography and tailored surface wettability, Langmuir 20 (2004) 7665–7669.
[20] C. Ukiwe, D.Y. Kwok, On the maximum spreading diameter of impacting droplets on well-prepared solid surfaces, Langmuir 21 (2005) 666–673.
[21] N.J. Shirtcliffe, G. McHale, M.I. Newton, G. Chabrol, C.C. Perry, Dual-scale roughness produces unusually water-repellent surfaces, Adv. Mater. 16 (2004) 1929–1932.
[22] W. Barthlott, C. Neinhuis, Purity of the sacred lotus, or escape from contamination in biological surfaces, Planta 202 (1) (1997) 1–8.
[23] L. Feng, S.H. Li, Y.S. Li, H.J. Li, L.J. Zhang, J. Zhai, Y.L. Song, B.Q. Liu, L. Jiang, D.B. Zhu, Super-hydrophobic surfaces: from natural to artificial, Adv. Mater. 14 (2002) 1857.
[24] X.F. Gao, L. Jiang, Biophysics: Water-Repellent Legs of Water Striders, Nature 432 (2004) 36.
[25] F. Shi, Z. Wang, X. Zhang, Combinig a layer-by-layer assembling technique with electrochemical deposition of gold aggregates to mimic the legs of water-striders, Adv. Mater. 17 (2005) 1005–1009.
[26] Z. Han, Z. Mu, W. Yin, W. Li, S. Niu, J. Zhang, L. Ren, Biomimetic multifunctional surfaces inspired from animals, Adv. Colloid Interfac. 234 (2016) 27–50.
[27] T. Sun, L. Feng, X. Gao, L. Jiang, Bioinspired surfaces with special wettability, Acc. Chem. Res. 38 (2005) 644–652.
[28] I. Ahmad, C. Kan, A review on development and applications of bio-inspired superhydrophobic textiles, Materials 9 (2016) 892.
[29] X. Yao, Y. Song, L. Jiang, Applications of bio-inspired special wettable surfaces, Adv. Mater. 23 (2011) 719–734.
[30] M. Liu, Y. Zheng, J. Zhai, L. Jiang, Bioinspired super-antiwetting interfaces with special liquid-solid adhesion, Acc. Chem. Res. 43 (2010) 368–377.
[31] S. Wang, K. Liu, X. Yao, L. Jiang, Bioinspired surfaces with superwettability: new insight on theory, design, and applications, Chem. Rev. 115 (2015) 8230–8293.
[32] Y. Deng, D. Mager, Y. Bai, T. Zhou, Z. Liu, L. Wen, Y. Wu, J.G. Korvink, Inversely designed micro-textures for robust Cassie–Baxter mode of super-hydrophobicity, Comput. Methods Appl. Mech. Eng. 341 (2018) 113–132.
[33] A. Cavalli, P. Boggilda, F. Okkels, Topology optimization of robust superhydrophobic surfaces, Soft Matter 9 (2013) 2234–2238.
[34] Y. Rahmawan, L. Xu, S. Yang, Self-assembly of nanostructures towards transparent, superhydrophobic surfaces, J. Mater. Chem. A 1 (2013) 2955–2969.
[35] X. Song, J. Zhai, Y. Wang, L. Jiang, Fabrication of superhydrophobic surfaces by self-assembly and their water-adhesion properties, J. Phys. Chem. B 109 (2005) 4048–4052.
[36] A. Pimpin, W. Srituravanich, Review on micro- and nanolithography techniques and their applications, Eng. J. 16 (2012) 37–55.
[37] M.P. Bendsoe, O. Sigmund, Topology optimization theory, methods and applications, Springer, Berlin, 2003.
[38] B. Lazarov, O. Sigmund, Filters in topology optimization based on Helmholtz type differential equations, Int. J. Numer. Methods Eng. 86 (2010) 765–781.
[39] T. Borrvall, J. Petersson, Topology optimization of fluid in stokes flow, Int. J. Numer. Meth. Fluids 41 (2003) 77–107.
[40] T. Nomura, K. Sato, K. Taguchi, T. Kashiwa, S. Nishiwaki, Structural topology optimization for the design of broadband dielectric resonator antennas using the finite difference time domain technique, Int. J. Numer. Meth. Eng. 71 (2007) 1261–1296.
[41] O. Sigmund, K.G. Hougaard, Geometric properties of optimal photonic crystals, Phys. Rev. Lett. 100 (2008) 153904.
[42] M.B. Duhring, J.S. Jensen, O. Sigmund, Acoustic design by topology optimization, J. Sound Vib. 317 (2008) 557–575.
[43] W. Akl, A. El-Sabbagh, K. Al-Mitani, Topology optimization of a plate coupled with acoustic cavity, Int. J. Solids Struct. 46 (2008) 2060–2074.
[44] A. Gersborg-Hansen, M.P. Bendsoe, O. Sigmund, Topology optimization of heat conduction problems using the finite volume method, Struct. Multidiscip. Optim. 31 (2006) 251–259.
[45] S. Zhou, W. Li, G. Sun, Q. Li, A level-set procedure for the design of electromagnetic metamaterials, Opt. Exp. 18 (2010) 6693–6702.
[46] S. Zhou, W. Li, Y. Chen, G. Sun, Q. Li, Topology optimization for negative permeability metamaterials using level-set algorithm, Acta Mater. 59 (2011) 2624–2636.
[47] M. Otomori, T. Yamada, K. Izui, S. Nishiwaki, J. Andkjær, A topology optimization method based on the level set method for the design of negative permeability dielectric metamaterials, Comput. Methods Appl. Mech. Eng. 237–240 (2012) 192–211.
[48] O. Sigmund, Materials with prescribed constitutive parameters: an inverse homogenization problem, Int. J. Solids Struct. 31 (1996) 2313–2329.
[49] Y. Deng, Z. Liu, P. Zhang, Y. Liu, Y. Wu, Topology optimization of unsteady incompressible Navier–Stokes flows, J. Comput. Phys. 230 (2011) 6688–6708.
[50] Y. Deng, Z. Liu, J. Wu, Y. Wu, Topology optimization of steady Navier–Stokes flow with body force, Comput. Methods Appl. Mech. Eng. 255 (2013) 306–321.
[51] L. Zhao, S. Ha, K.W. Sharp, A.B. Geltmacher, R. W. Fonda, A.H. Kinsey, Y. Zhang, S.M. Ryan, D. Erdeniz, D.C. Dunand, K.J. Hemker, J.K. Guest, T.P. Weihs, Permeability measurements and modeling of topology-optimized metallic 3-d woven lattices, Acta Mater. 81 (2014) 326–336.
[52] J. Toster, D. Lewis, Investigation of roughness periodicity on the hydrophobic properties of surfaces, Aust. J. Chem. 68 (2015) 1228–1232.
[53] T. Young, An essay on the cohesion of fluids, Phil. Trans. R. Soc. Lond. (95) (1805) 65–87.
[54] P. Laplace, Supplement to the tenth edition, Méchanique céleste 10 (1806) 1985–1990.
[55] K. Yosida, Functional Analysis, Springer, Berlin, 1980.
[56] B. Lazarov, O. Sigmund, Filters in topology optimization based on Helmholtz type differential equations, Int. J. Numer. Methods Eng. 86 (2011) 765–781.
[57] F. Wang, B.S. Lazarov, O. Sigmund, On projection methods, convergence and robust formulations in topology optimization, Struct. Multidiscip. Optim. 43 (2011) 767–784.
[58] J. Guest, J. Prevost, T. Belytschko, Achieving minimum length scale in topology optimization using nodal design variables and projection functions, Int. J. Numer. Methods Eng. 61 (2004) 238–254.
[59] M. Hinze, R. Pinnau, U. M, S. Ulbrich, Optimization with PDE Constraints, Springer, Berlin, 2009.
[60] K. Svanberg, The method of moving asymptotes: a new method for structural optimization, Int. J. Numer. Meth. Eng. 24 (1987) 359–373.
[61] G. McHale, N.J. Shirtcliffe, M.I. Newton, Contact-angle hysteresis on super-hydrophobic surfaces, Langmuir 20 (2004) 10146–10149.
[62] B. Eral, D.J.C.M.t. Mannetje, J.M. Oh, Contact angle hysteresis: a review of fundamentals and applications, Colloid. Polym. Sci. 291 (2013) 247–260.